Automated multiwell fluorescence lifetime imaging for Förster resonant energy transfer assays and High Content Analysis

Journal:	*Analytical Methods*
Manuscript ID:	AY-ART-01-2015-000244.R1
Article Type:	Paper
Date Submitted by the Author:	22-Mar-2015

Complete List of Authors:	Kelly, Douglas; Photonics group, Imperial College London, Department of Physics Warren, Sean; Photonics group, Imperial College London, Department of Physics Alibhai, Dominic; Insitute of Chemical Biology, Imperial College London, Department of Chemistry Kumar, Sunil; Photonics group, Imperial College London, Department of Physics Alexandrov, Yuriy; Photonics group, Imperial College London, Department of Physics Munro, Ian; Photonics group, Imperial College London, Department of Physics Margineanu, Anca; Photonics group, Imperial College London, Department of Physics McCormack, Jessica; National Heart and Lung Institute, Imperial College London, Faculty of Medicine Welsh, Natalie; National Heart and Lung Institute, Imperial College London, Faculty of Medicine Serwa, Remigiusz; Chemical Biology Section, Imperial College London, Department of Chemistry Thinon, Emanuelle; Chemical Biology Section, Imperial College London, Department of Chemistry Kongsema, Mesayamas; Imperial College London, Department of Surgery and Cancer McGinty, James; Photonics group, Imperial College London, Department of Physics Talbot, Clifford; Photonics group, Imperial College London, Department of Physics Murray, Edward; Retroscreen Virology Ltd, Stuhmeier, Frank; Pfizer Limited, Pfizer Global Research and Development Neil, Mark; Photonics group, Imperial College London, Department of Physics Tate, Edward; Chemical Biology Section, Imperial College London, Department of Chemistry Braga, Vania; National Heart and Lung Institute, Imperial College London, Faculty of Medicine

	Lam, Eric; Imperial College London, Surgery and Cancer Dunsby, Christopher; Photonics group, Imperial College London, Department of Physics; Centre for Histopathology, Imperial College London, French, Paul; Photonics group, Imperial College London, Department of Physics

Journal Name

RSCPublishing

ARTICLE

Automated multiwell fluorescence lifetime imaging for Förster resonance energy transfer assays and High Content Analysis

Cite this: DOI: 10.1039/xoxxoooooox

Received ooth January 2012,
Accepted ooth January 2012

DOI: 10.1039/xoxxoooooox

www.rsc.org/

Douglas J. Kelly[a], Sean C. Warren[a], Dominic Alibhai[b], Sunil Kumar[a], Yuriy Alexandrov[a], Ian Munro[a], Anca Margineanu[a], Jessica McCormack[c], Natalie J. Welsh[c], Remigiusz A. Serwa[d], Emmanuelle Thinon[d], Mesayamas Kongsema[e], James McGinty[a], Clifford Talbot[a], Edward J. Murray[f], Frank Stuhmeier[g], Mark A. A. Neil[a], Edward W. Tate[d], Vania M. M. Braga[c], Eric W.-F. Lam[e,] Christopher Dunsby[a,h] and Paul M. W. French[a]

Fluorescence lifetime measurements can provide quantitative assays of the local fluorophore environment and can be applied to read out biomolecular interactions via Förster resonance energy transfer (FRET). Fluorescence lifetime imaging (FLIM) can be automated for high content analysis (HCA) to map protein-protein interactions with applications in drug discovery, systems biology and basic research. The automated acquisition of FLIM data over 100's of fields of view provides statistical power to overcome noise in instrumentation and biological systems and thus exploit relatively small changes in mean lifetime to provide useful readouts that would not be practically achievable in manual microscopy experiments. We present here an automated HCA system with the ability to perform rapid unsupervised optically sectioned FLIM of fixed and live biological samples and illustrate its potential through exemplar applications of different FRET readouts.

Introduction to FLIM HCA

The trend towards automated high content assays in drug discovery is increasingly being mirrored by the use of automated microscopy systems for basic research in the life sciences. The ability to rapidly assay and analyse 100's to 1000's of fields of view provides a statistical power not achievable in manual experiments with 10's of dishes of cells typically imaged with conventional microscopes, and the automation of image data acquisition and analysis is a significant step towards eliminating operator bias and random noise in both instrumentation and biological samples. Further, large sample arrays can often be designed to detect or eliminate systematic errors. While many imaging modalities are being applied in automated high content analysis (HCA), fluorescence based techniques are of particular interest because of the specificity of labelling that is achievable, e.g. using antibodies or genetically expressed fluorescent proteins. Today most commercially available instruments feature fluorescence intensity imaging in one or more spectral channels to map the relative distribution and co-localization of labelled proteins.

There is increasing interest in using fluorescence-based readouts to provide information on biological processes occurring on scales below the spatial resolution of fluorescence microscopes – essentially by probing the local molecular environment using fluorophores as sensors in biological samples. Endogenous fluorophores, including some cellular metabolites and extracellular matrix components, can provide intrinsic readouts of biological processes and pathologies while exogenous molecularly-specific labels, particularly genetically expressed fluorophores, can provide readouts of protein interactions and therefore of cell signalling processes. In biology laboratories it is now common to utilize Förster Resonance Energy Transfer (FRET) measurements in fluorescence microscopes to probe protein interactions by

detecting (and sometimes quantifying) the close proximity of specific fluorophore labels. FRET readouts can thus provide maps of protein interactions through measurements of the fluorophore populations in each image pixel. FRET entails exciting a "donor" fluorophore and observing the consequences of a resonant transfer of the excitation state to an appropriate "acceptor" fluorophore. This energy transfer is mediated by a direct dipole-dipole interaction and only occurs between fluorophores separated by less than ~10 nm[1], enabling the detection and measurement of the close proximity of appropriately labelled proteins – either as an end point in fixed cells or as a dynamic event in live cells. This can be used to assay interactions between proteins, for example by intermolecular FRET of proteins binding or aggregating, as illustrated in Fig. 1(a, b). Alternatively intramolecular FRET can be used to read out conformational changes, binding or cleaving of single molecular constructs labelled with both donor and acceptor fluorophores as illustrated in Fig. 1(c, d, e). The latter is the basis of a range of genetically expressed intracellular biosensors[2] for analytes such as calcium, potassium and chloride ions and signalling molecules such as IP_3, PIP_2 and caspase, among others.

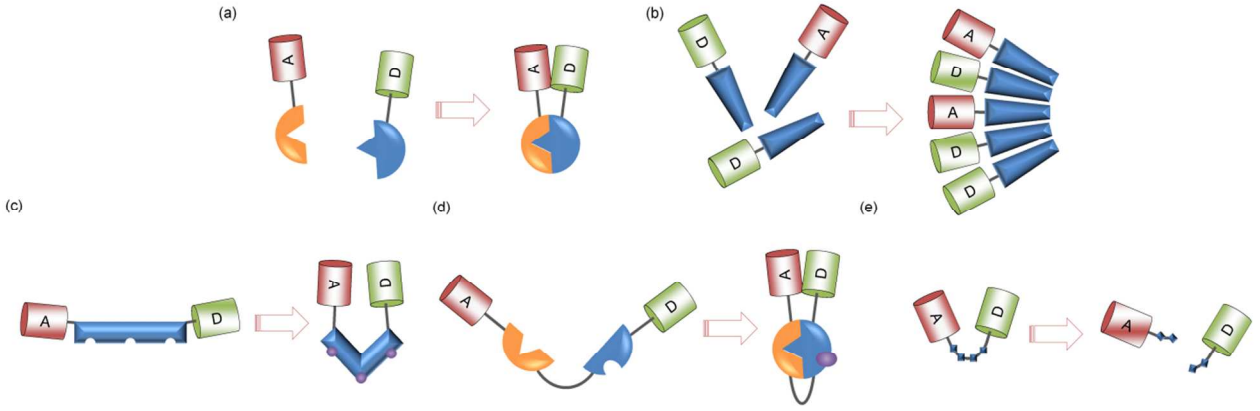

Fig. 1 (a) Intermolecular FRET biosensor where FRET increases on binding events. (b) Intermolecular FRET reporting aggregation of a (stochastically labelled) protein. (c) Intramolecular FRET biosensor where FRET increases due to conformational change on ligand binding. (d) Intramolecular FRET biosensor where FRET increases due to binding event on protein activation. (e) Intramolecular FRET biosensor where FRET decreases upon cleavage by proteinase.

Imaging techniques that can map molecular interactions by reading out FRET are desirable to readout such biosensors or to reveal the spatio-temporal organization of proteins within cells, e.g. to provide readouts of cell signalling. Automating such imaging techniques can enable such readouts to be exploited for assays including screens of libraries of reagents or siRNA gene knockdowns, and for systems biology studies; thus HCA FRET instrumentation could find significant application in drug discovery and basic research in the life sciences.

While there are many approaches to map FRET[3], the most widely used are probably spectral ratiometric imaging, where FRET is indicated by the relative increase in the ratio of acceptor to donor intensity, and fluorescence lifetime imaging (FLIM) where the relaxation of fluorophores from their excited state through FRET results in a decrease in the donor fluorescence lifetime. Spectrally-resolved imaging of the donor and acceptor emission typically requires fewer detected photons per pixel and so provides faster imaging than FLIM, but quantitative spectrally-resolved measurements require additional control samples labelled with donor only and acceptor only to calibrate the spectral response of the system – which includes the instrument and the sample itself (inner filter effect) – and to account for spectral cross-talk (direct excitation of the acceptor and spectral bleed-through). Spectral ratiometric FRET measurements can then yield the relative proportion of donor and acceptor molecules and the *effective FRET efficiency* (i.e. product of actual FRET efficiency and fraction of FRETing donor/acceptor molecules)[4]. When the donor/acceptor stoichiometry is known – as is the case when using single molecule FRET biosensors – this approach can provide a quantitative readout. If the fractions of the FRETing donor and acceptor populations are required, e.g. for studies of dose response, an independent measurement of the actual FRET efficiency is also necessary – usually provided by measuring a known (positive) FRET control sample or by measuring the FRET efficiency using a different analysis method such as acceptor photobleaching or FLIM.

Fluorescence lifetime measurements of FRET are inherently ratiometric and so are independent of fluorophore concentration, excitation and detection efficiencies and the impact of scattering and sample absorption[5]. Furthermore, since only measurements of the donor emission are required, they avoid the need for spectral calibration and are not subject to cross-talk so fluorescence lifetime-based FRET measurements can be readily compared across different instruments and samples – potentially including between cell-based assays and endoscopy or tomography of live disease models[6]. In principle, FRET efficiencies and population fractions can be directly obtained by fitting donor fluorescence decay profiles to an appropriate multi-exponential decay model – subject to sufficient signal to noise ratio. Besides FRET, FLIM can also be used to map other variations in local fluorophore

environment, e.g. reporting on the concentration of analytes such as calcium using fluorescent dyes or on physical changes such as temperature or membrane lipid order. In spite of these advantages, however, FLIM has not yet made a significant impact on drug discovery or systems biology, partly due to a lack of available FLIM instrumentation for automated multiwell plate readouts. FLIM is most commonly implemented using laser scanning microscopes with time correlated single photon counting (TCSPC) and the sequential pixel acquisition of this approach typically results in data acquisition times of 10's - 100's of seconds per cell, depending on the sample brightness. Such acquisition times are undesirable or impractical for HCA where 100's-1000's of fields of view are to be imaged and, if the excitation intensity is increased to permit much faster imaging, there are significant issues with photobleaching and phototoxicity. TCSPC has been implemented in a laser scanning multiwell plate reader[7] that did not acquire fluorescence lifetime images but instead delivered a single lifetime measurement per well. Recently an imaging multiwell plate reader was reported that did implement multiphoton TCSPC FLIM but this was utilised for secondary experiments following identification of "hits" by steady-state polarisation-resolved anisotropy imaging, since FLIM was considered to be too slow for rapid measurements[8]. Polarisation resolved anisotropy imaging is an alternative ratiometric technique to map FRET that exploits the decrease in fluorescence anisotropy of the acceptor in the presence of FRET. While this can reach similar imaging speeds to spectral ratiometric imaging, it is also sensitive to spectral cross-talk (e.g. direct excitation of the acceptor and detection of donor emission in the acceptor spectral channel) and requires calibration to account for polarisation cross talk and so does not directly provide the FRET efficiency. As such it has been implemented to provide qualitative readouts of FRET in plate readers and laser scanning cytometers.

To realise the advantages of FLIM for HCA, we have developed an automated rapid (~10s/field of view) FLIM multiwell plate reader that is described below together with exemplar FRET based-assays. Our realization of rapid FLIM and FRET for HCA has been achieved using wide-field time-gated imaging. Where optical sectioning is required, this can be realised using a quasi-wide-field optically sectioning Nipkow ("spinning disc") microscope scanner[9]. Wide-field FLIM achieves faster imaging rates than single-beam scanning TCSPC with lower photobleaching due to the parallel pixel interrogation and we have previously reported optically sectioned FLIM-FRET of live cells at up to 10 frames/s[9]. It is also possible to implement wide-field FLIM using frequency domain techniques that utilise either a modulated optical intensifier[10] or a CMOS camera with modulated gain[11]. Frequency domain and time domain FLIM can provide equivalent information although there are performance trade-offs with specific implementations of both approaches (see reference 3 and citations therein for further discussion of FLIM and FRET).

The first HCA instrument for unsupervised FLIM of multiwell plate sample arrays[12] utilised frequency domain fluorescence lifetime determination of FRET in a wide-field (non-sectioning) microscope, demonstrating the potential of automated FLIM-FRET and the statistical analysis of FLIM array data. This was followed by the first optical sectioning automated high-speed FLIM multiwell plate reader[13] for HCA (utilising time-gated imaging in a Nipkow disc microscope) that realised unsupervised FLIM-FRET of fixed and live cells with acquisition times of less than 10 s per well including sample translation, autofocus, cell finding and system calibration. Subsequently a wide-field (non-sectioning) frequency domain FLIM plate reader was applied to image post translational modifications (tyrosine phosphorylation) *in situ* – specifically uncovering components that transduce signals from epidermal growth factor receptors[14] and illustrating the potential biological impact of FLIM HCA. Our time-gated optical sectioning FLIM approach was applied to an exemplar FLIM FRET assay of HIV-1 Gag aggregation modelled by the formation of virus-like particles implemented first in live HEK293T cells using a commercial wide-field multiwell plate reader (GE Healthcare INCell 1000) modified for FLIM[6] and then in fixed HeLa cells using a motorised widefield microscope (Olympus IX81-ZDC) adapted for FLIM[15]. These instruments typically provided unsupervised automated FLIM of cells labelled with fluorescent proteins at rates faster than 10 s per field of view (FOV), acquiring the actual FLIM data in a few seconds with the remaining time being required to move between different FOV and to refocus the microscope. Thus 100's of FOV can be readily acquired in 10's of minutes.

At this imaging speed we typically acquire several hundred photons/pixel, which is sufficient to fit fluorescence decay profiles to a mono-exponential decay model on a per-pixel basis and obtain a measure of FRET via the change in effective lifetime. For the assay of HIV-1 Gag aggregation, we read out changes in the mean donor lifetime of ~100 ps correlated with biological controls and achieved Z' of > 0.6 in dose response studies with NMT inhibitors of myristoylation of the Gag protein, which is a prerequisite of aggregation. This performance is possible because of the large number of cells over which the data can be analysed, which enables useful readouts to be realised using much smaller changes in fluorescence lifetime than is possible with the typical numbers of cells imaged in manual microscopy experiments.

While approximating experimental fluorescence decay profiles to a single exponential model is useful for many applications, it is often desirable to obtain more quantitative information by fitting to complex fluorescence decay models, which typically requires tens of thousands of photons for reliable fitting. We address this challenge by applying global analysis to such FLIM data. The simplest approach we implement is "global binning", which involves summing all the detected photons from a FOV - or from a region of interest (ROI) - and fitting the resulting decay profile to a the complex model, under the assumption that the fluorescence lifetime components are invariant across the image. For FRET assays one can fit

globally binned data to a double exponential decay model to obtain the lifetimes of the FRETing and non-FRETing components and then refit the data pixel-wise with these lifetimes fixed to determine the population fraction of each component in each pixel. In a second approach, which we describe as 'global fitting', the lifetimes and contributions are fitted simultaneously across a whole FOV – or across a data set that could comprise multiple FOVs, e.g. from a multiwell plate experiment or a time series of images. The global fitting approach is able to exploit the spatial variation of contributions across the image that is lost in the global binning approach, providing stronger constraints on the lifetime estimates, albeit at the cost of significantly more computation, and therefore more reliable results[16]. Historically, the main disadvantage of global fitting of lifetime data has been the significant time and computational power required. We have developed an open source software tool called *FLIMfit*[17] that it is able to rapidly analyse multiwell plate FLIM datasets on conventional PC workstations. For example, a multiwell time-gated FLIM dataset with five time gates acquired for each of 394 FOV, with each image containing 672 x 512 pixels, required 32 seconds and 2 GB of memory to analyse globally. *FLIMfit* utilises a separable nonlinear least square fitting algorithm implemented using multithreaded parallel algorithms to enable effective scaling on multicore processors and its code has been optimised to minimise memory usage. Besides analysing FLIM FRET data, this global analysis tool can also be applied other complex models such as polarisation-resolved fluorescence decay profiles.

This article describes the experimental configuration of our automated wide-field or optically sectioning FLIM multiwell plate reader and presents its application to exemplar FRET assays of cellular signalling processes using intermolecular and intramolecular FRET. This instrument builds on the hardware and software tools previously reported[13,15,17] and the configurations utilised for the work reported here are described in the Methods section below.

Results: FLIM HCA of FRET assays

Intermolecular aggregation FRET assay: oligomerisation of HIV-1 Gag protein

The first exemplar assay follows on from previous work[15] on the use of FLIM FRET to assay the oligomerisation of HIV-1 Gag - the molecular machine responsible for orchestrating the assembly of nascent HIV-1 virions[18] In the absence of other viral proteins and enzymes, expression of HIV-1 Gag alone results in the production of viral-like particles (VLPs) that are similar to immature HIV-1 virions and are often used as a model system for late stages in the HIV-1 lifecycle. The membrane binding of HIV-1 Gag, which is a prerequisite for HIV (and VLP) assembly, is thought to operate through a 'myristic switch' mechanism[19]. Monomers of Gag contain a sequestered myristic acid moiety (a co-translational modification to the Gag protein) that is exposed to the solvent upon dimerization of two or more Gag proteins, with the resulting increase in hydrophobicity driving membrane binding. The HIV-1 Gag protein used in this work has a C-terminal fluorescent protein tag (either CFP or YFP) added to enable Gag distribution to be visualized and VLP formation to be studied via FLIM-FRET as the Gag oligomerisation brings the FRET donors and acceptors into close proximity, as illustrated in Fig. 2. To obtain a quantitative evaluation of the FLIM-FRET assay of Gag oligomerisation, we systematically disrupt the endogenous enzymes responsible for the addition of the myristic acid to Gag through the use of an N-myristoyltransferase inhibitor[20] (NMT inhibitor; DDD85646) thereby generating dose response curves from which IC50 values can be calculated.

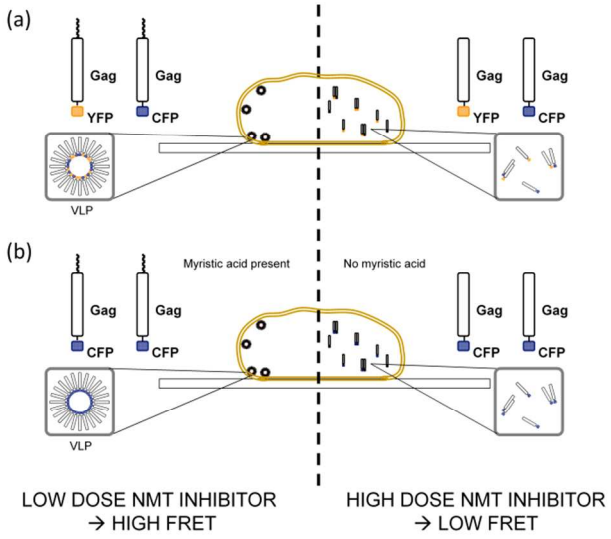

Fig. 2 Schematic of (a) Gag protein labelled with CFP or YFP: left - aggregating at the cell membrane and right - dimerising in the cytosol; (b) Gag protein labelled only with CFP: left - aggregating at the cell membrane and right - dimerising in the cytosol.

An interesting outcome of our previous study[15] was that homoFRET lifetime readouts (for which HeLa cells were transfected only with HIV-1 Gag-CFP) provided superior performance (in terms of Z') compared to heteroFRET between Gag-CFP and Gag-YFP. The lifetime change due to homoFRET between CFP molecules occurs because CFP is thought to exist in a slow equilibrium between a number of different molecular conformations with distinct lifetimes. Energy transfer between these species leads to a reduction in the mean lifetime[21,22]. The CFP homo-FRET readout has several advantages over CFP/YFP hetero-FRET including simplifying sample preparation as well as increasing spectral efficiency, which could be important for multiplexed readouts. We note that the decay profile resulting from CFP alone is complex and undergoing FRET is expected to have more than 4 components (i.e. at least two sets of FRETing and non-FRETing donor lifetimes). In this case of oligomerisation, each CFP donor may FRET with more than one acceptor and this will add further complexity to the donor decay. Therefore we

choose to represent this complex behaviour by fitting to a single exponential decay model, which simplifies the data analysis and enables direct comparisons with our previously published work[15]where a monoexponential decay model was shown to provide excellent quantitative results in the inhibitor assay.

Our previous published study presented results from assays of fixed cells and here in Fig. 3 we present results of an assay of the effectiveness of an NMT inhibitor undertaken in live HeLa cells[23] using both hetero-FRET and homo-FRET readouts that were implemented by seeding a well plate with cells either expressing Gag-CFP alone or co-expressing Gag-CFP and Gag-YFP. These cells were incubated with varying concentrations of the NMT inhibitor, as shown in the plate scheme in Fig. 3(a), from 10 µM to 0.001 µM. Fig. 3(b) presents exemplar fluorescence lifetime images of these labelled cells and Fig. 3(c) presents the map of mean CFP lifetimes for each well (fitted to a single exponential decay model). This shows the general trend of increasing lifetime (decreasing FRET) with increasing NMT inhibitor dose for both the hetero-FRET (Gag-CFP + Gag-YFP) case, and the homo-FRET (Gag-CFP only) case. To provide a positive control, column 1 contained cells transfected with myristic acid negative mutants of HIV-1 Gag[19] that are unable to bind the plasma membrane: $^{Myr(-)}$Gag-CFP or $^{Myr(-)}$Gag-CFP + $^{Myr(-)}$Gag-YFP. To provide a negative control, column 11 contained the respective Gag proteins treated with only the DMSO vehicle.

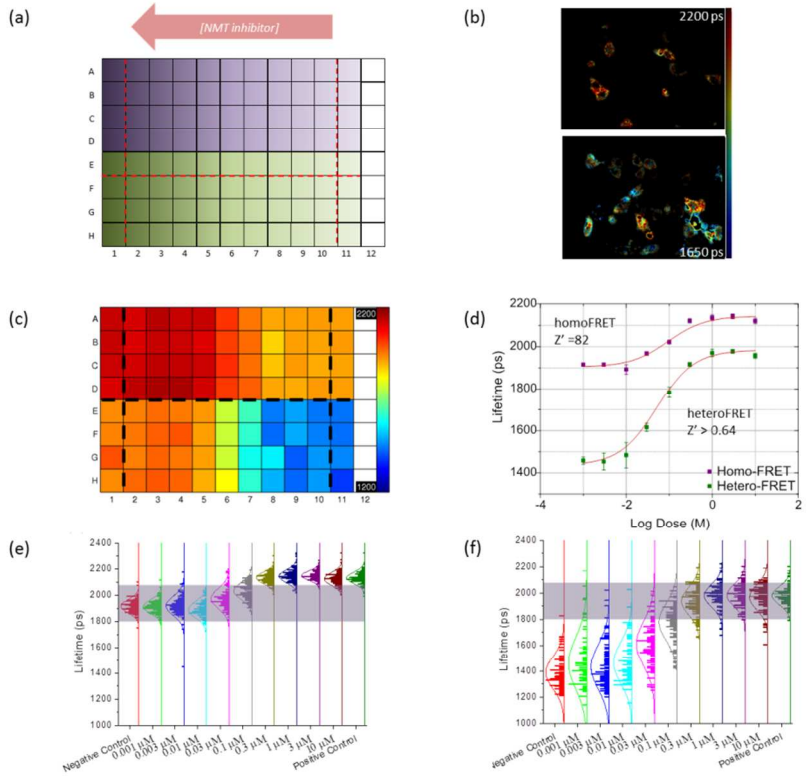

Fig. 3 FLIM FRET assay of virus-like particle formation in live HeLa cells at 37°C transfected with Gag-CFP (top half of plate) and Gag-CFP/Gag-YFP (lower half). (a) Plate map showing NMT inhibitor concentration. (b) Exemplar fluorescence lifetime images acquired. (c) Heat map of mean fluorescence lifetime averaged over all FOV in each well. (d) Dose response curves showing reduction in FRET linked to inhibition of Gag myristoylation upon treatment with NMT inhibitor for homoFRET and heteroFRET readouts. Population histograms of mean lifetimes over segmented cell membranes per condition for (e) homoFRET and (f) heteroFRET readouts

Figure 3(d) presents the corresponding hetero-FRET and homo-FRET dose response curves for which all the pixel lifetimes in the repeat wells (each with 4 FOVs) were averaged for each concentration of NMT inhibitor (DDD85646) and the average value per well was plotted against log[dose], with the error bars determined from the standard deviation between wells. These dose response curves result in calculated IC50 values of 59 and 91 nM for the hetero-FRET and homo-FRET data when fitted to a 3PL model, comparable to those obtained in a recent chemical proteomics study of NMT inhibitors carried out in HeLa cells[24], which showed the IC50 value of DDD85646 to be 170 ± 31 nM.

We note that these lifetime values are considerably lower than those we reported with the fixed cell assay[15]. This is because the fixed cell assay was undertaken at room temperature (~23°C) and CFP presents a significant temperature dependence of fluorescence lifetime, which has been shown to vary by up to 50 ps per degree[25,26]. As observed with the fixed cell assay[15], Fig. 3(d) also presents an offset in the homo- and hetero-FRET lifetimes – including in the homo- and hetero-FRET positive control wells (column 1). This is attributed to the residual FRET between dimerising Gag proteins within the cytoplasm that produces a larger decrease in CFP lifetime for the heteroFRET case.

The Z' values for the homo- and hetero-FRET assays were found to be 0.82 and 0.64 respectively, indicating a separation of positive and negative controls that is considered "excellent" for a pharmaceutical assay. These Z' values are higher than those obtained with the fixed cell assay, which may be attributed to the homeostasis in live cells maintaining a more consistent fluorophore environment and possibly to effects of fixation on the measured lifetimes of the fluorescence proteins. It is also possible that the temperature was more precisely controlled for the live cell assay.

To further explore the difference between the heteroFRET and homoFRET assays and to understand the underlying variability in the cell populations, we applied image segmentation to the data presented above, selecting the plasma membrane as a region of interest since this is where the Gag oligomerisation occurs. Fig. 3(e, f) shows the results of binning all the pixels within each cell membrane ROI and fitting to a single exponential decay model to yield a single lifetime value per cell. This data is plotted as a histogram with a bin size of 5 ps from 1000 to 2400 ps (a total 280 bins) and a normal distribution model is overlaid onto the data. Fig. 3(e) shows that the homo-FRET assay displays a relatively narrow distribution around the mean lifetime value for each condition compared to the hetero-FRET shown in Fig. 3(f). This illustrates the effects of the variable donor-acceptor stoichiometry of the hetero-FRET assay. The identical purple overlay areas in Fig. 3(e, f) correspond to the approximate distribution of the negative control data from the homo-FRET plate. In Fig. 3(f) the outliers for the lowest inhibitor doses in the hetero-FRET plate match the negative control data for Gag-CFP transfected cells – indicating cells where there is negligible Gag-YFP expressed. This figure highlights the additional complications inherent within the hetero-FRET assay and shows how the use of CFP-based homoFRET readouts can facilitate improved assay quantification as well as simplifying the production of the sample arrays and reducing reagent costs. It is important to understand, however, that the lifetime change of CFP upon homoFRET could also present problems for FRET experiments, e.g. when using single molecule FRET biosensors. If there is a high concentration of the FRET biosensor within the cell, then homoFRET between the donor CFP of different biosensors could lead to false positive readouts of shorter donor lifetime.

To summarise, we have demonstrated the improved quantification of an assay of HIV-1 Gag protein oligomerisation implemented with live cells and the benefits of homoFRET based lifetime readouts using CFP. We note that the Z' demonstrated in these assays exceed the requirements for use in the pharmaceutical industry and confirm that such assays of protein aggregation could be used for drug screening.

Intermolecular protein binding FRET assay: SUMOylation of FOXM1 protein

The second exemplar FRET assay addresses drug response in the context of refractory cancer - specifically the post-translational modification of the transcription factor FOXM1 by the small ubiquitin-like modifier protein SUMO1 and its sensitivity to anthracyclines, which are potential therapeutic agents for breast cancer[27]. The forkhead box M1 (FOXM1) protein is a transcription factor, the dysregulation of which is linked to aberrant cell behaviour relating to unchecked cell cycle progression and proliferation. If FOXM1 is depleted, the progress of cells through the cell cycle is disrupted and consequent mitotic abnormalities can result in aneuploidy or polyploidy[28]. Conversely, overexpression of FOXM1 is linked to tumorigenesis, angiogenesis and metastasis[29,30]. In addition to its role in tumorigenesis, progression and metastasis, FOXM1 is also implicated in drug resistance in cancer cells and its expression levels have been associated with anthracycline resistance. Doxorubicin is an anthracycline used in chemotherapy and it has been reported that doxorubicin-resistant breast cancer carcinoma cell lines (MCF7-DoxR), generated from wild type MCF7 by selection pressure under long term treatment with doxorubicin, exhibit enhanced expression of FOXM1[31]. Sensitivity to doxorubicin can be restored to these resistant cell lines by depleting FOXM1 using siRNA, and modulation of FOXM1 expression in response to anthracycline treatment varies between resistant and sensitive cells[30]. The mechanisms underlying this drug resistance are not yet understood but it is thought that anthracycline modulates FOXM1 activity through post-translational modifications and it has been shown that phosphorylation[32,33] and SUMOylation[34] occur in response to anthracycline treatment.

SUMOylation is the addition of a small ubiquitin-like modifier (SUMO) to a protein and is a peptide post-translational modification, closely related to ubiquitination. The potential role that that SUMOylation plays in modulating FOXM1 activity was investigated previously, primarily using biochemical techniques following cell fractionation such as His tag purification, co-immunoprecipitation (co-IP) and Western blotting[34]. This work served to illustrate the inhibitory effect on FOXM1 activity conferred by SUMOylation, including enhanced ubiquitination and degradation of FOXM1 and promotion of FOXM1 translocation to the cytoplasm. In addition, treatment with epirubicin (another anthracycline agent for chemotherapy) was shown to increase FOXM1 SUMOylation in MCF7 cells, highlighting the role of this modification in DNA damage response. Negative controls for these studies were realised using a "non-SUMOylatable" FOXM1 mutant, generated by performing five lysine-to-arginine mutations at the five SUMO-acceptor ΨKxE motifs present on FOXM1[34]. The resulting mutant (FOXM15X(K>R) (K201R/K218R/K460R/K478R/K495R), hereafter denoted as "FOXM1mut") was shown not to be modified by SUMO in Western blot analysis[34]. Expression of FOXM1mut enhanced proliferation compared to the active FOXM1, was more efficient in conferring resistance to anthracycline treatment, and exhibited different subcellular localisation compared to the wild-type[34].

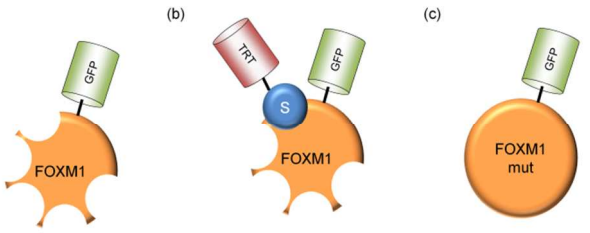

Fig. 4 Schematic representations of FOXM1-SUMOylation experiment fluorescent constructs. (a) Active FOXM1-eGFP. (b) SUMO1-TagRFP-T, binding at a FOXM1 SUMOylation consensus site. (c) Non-SUMOylatable FOXM15x(K>R)-eGFP.

The mechanisms by which this regulation of FOXM1 occurs are currently not well understood and this prompted our exploration of automated FLIM FRET HCA as a tool to study the dynamics of the SUMOylation in live cells in response to anthracycline treatment[35]. To this end FRET readouts of FOXM1-SUMOylation were implemented in live MCF7 breast cancer cells utilising the fluorescent constructs shown in Fig. 4 and assayed in response to a time course of treatment with doxorubicin. This is the first reported live cell FRET experiment investigating SUMOylation of FOXM1, which validates previous results that were obtained using biochemical measurements and FLIM of fixed cells[34]. For these experiments both wild type and non-SUMOylatable FOXM1mut were labelled with eGFP at the N-terminal end to act as FRET donors, while SUMO1 was labelled with TagRFP-T (subsequently denoted TRT) to act as the FRET acceptor. FOXM1 was selected to be labelled with the donor fluorophore rather than SUMO1 since the relative ubiquity of SUMO1 expression and the consequent surplus of acceptor fluorophores means that this should maximise the observable changes in donor lifetime.

Before undertaking the assay of SUMOylation dynamics, we first undertook preliminary experiments to establish that the background fluorescence (from endogenous cellular fluorophores, from growth media, from the plastic well plates used and from the doxorubicin) was low compared to the GFP fluorescence. We observed this background to be less than 10% of the typical GFP signal and, imaging wells with wild-type cells in the GFP channel, observed that this background signal level did not change with time or with doxorubicin treatment. We also undertook a study to confirm that there was no change in GFP fluorescence lifetime from non-specific interaction between the donor and acceptor fluorophores. For this we transfected MCF7 cells with free TRT alongside either FOXM1-eGFP or FOXM1mut-eGFP signal and observed no decrease in eGFP donor lifetime.

Fig. 5 (a) shows the plate map for the assay of FOXM1 SUMOylation dynamics, indicating the transfections and doxorubicin treatment for each well of a 96 well plate. Fig. 5 (b) shows the mean fluorescence lifetime heat map for a monoexponential fit to the donor fluorescence decay profile (taking into account the instrument response function and background signal) and Fig. 5 (c) shows representative fluorescence lifetime images of cells over the time course. The change in donor lifetime throughout the time course of doxorubicin treatment for each transfection condition is shown in Fig. 5 (d), for which the points represent the mean fluorescence lifetime of all the segmented cell images corresponding to a particular condition at a given time point. Only in the case when wild-type FOXM1-eGFP is cotransfected with SUMO1-TRT (triangles) is there a significant deviation from the zero time point with treatment (where significance was assessed using Dunnett's test). In this case, the fitted lifetime is found to decrease significantly for treatments between 6 and 8 hours, followed by a return towards the zero time point value by 21 h post-treatment. Thus the FLIM FRET data from wells in which wild-type FOXM1-eGFP is cotransfected with SUMO-TRT indicates a significant decrease in measured donor lifetime when cells have been exposed to doxorubicin treatment for between 6 and 8 hours, which is attributed to DNA damage incurred by the anthracycline treatment over the time course. In contrast, the non-SUMOylatable mutant FOXM1 construct does not show a change in donor lifetime over the time course of anthracycline treatment, as expected. This observation is consistent with co-IP assays, which confirmed that FOXM1-SUMOylation occurs by 6 hours, resulting in the formation of higher-order complexes[34]. We note that these biochemical studies have indicated that SUMOylation of FOXM1 also accelerates degradation of the transcription factor[34]; this degradation may explain the decrease in FOXM1-SUMO1 interaction (as indicated by the reduced change in donor lifetime) evident at 21 and 24 hour time points in the FLIM-FRET assay. Furthermore, caspase-mediated cleavage of the N-terminus of FOXM1[36] may act to reduce FRET signal between the donor and acceptor fluorescent proteins if apoptosis is induced by anthracycline treatment over these timescales[37].

To provide a more quantitative indication of the degree of FOXM1 SUMOylation as a function of time, all the data at each time point was globally fitted to a double exponential decay model of the donor fluorescence across all the FOXM1-eGFP wells and all the FOXM1mut-eGFP wells separately. To provide a more quantitative indication of the degree of FOXM1 SUMOylation as a function of time, all the data at each time point was globally fitted to a double exponential decay model of the donor fluorescence across all the FOXM1-eGFP wells and all the FOXM1mut-eGFP wells separately. In this case, short and long lifetime components correspond to FRETing and non-FRETing (SUMOylated and non-SUMOylated) FOXM1, respectively. This model fitted the data with a lower chi^2 than a monoexponential fit. This approach yielded mean lifetimes of the long and short components of 2770 ps and 2034 ps for the FOXM1-eGFP donor and 2800 ps and 2134 ps for the FOXM1mut-eGFP donor. Fig. 5 (e) shows the corresponding population fraction of the short lifetime component (i.e. FRETing donor) for wells containing both donor and acceptor constructs. Significant deviation from the untreated case is seen in the wild-type FOXM1-eGFP case at 6 h and 8 h doxorubicin treatment (Dunnett's test). We note that the application of a

biexponential fitting model to the lifetime data, as used to generate Fig. 5 (e), should be treated with caution since active FOXM1 may be SUMOylated on multiple sites and both active and mutated FOXM1 may interact with the acceptor construct via multiple SUMO1 interaction motifs. This could result a range of FRET efficiencies for different interactions and therefore in more complex decay profiles than a double exponential model.

It is notable that the donor-only lifetimes obtained for FOXM1-eGFP and FOXM1mut-eGFP are longer than those typically obtained for free eGFP. However, the mean lifetime obtained for the wells transfected with free eGFP in place of the FOXM1 constructs (i.e. columns 9-12) returned a mean lifetime of 2367 ps, which is in the familiar range for eGFP. This gives us confidence that the observed changes in lifetime are not artefacts and that the longer lifetime of the FOXM1 constructs is a consequence of the local molecular environment of the fluorophore in these constructs.

A further point to note is that, while only the active FOXM1-eGFP donor construct in the presence of the SUMO-TRT acceptor presents a change in donor lifetime as a consequence of treatment with doxorubicin, the lifetime of the FOXM1mut-eGFP donor in the presence of SUMO-TRT is significantly shorter than that of the active FOXM1 donor before treatment with doxorubicin. This could be attributed to a higher baseline level of interaction between mutated FOXM1 and SUMO1 compared to active FOXM1 and SUMO1, possibly due to non-covalent FOXM1 interactions with SUMO-interacting motifs (SIMs). The higher base line is suggested by the observed lifetime difference over the whole time course between conditions in which FOXM1mut-eGFP is transfected with and without SUMO1-TRT. These observations suggest that there is some DNA damage response-independent mechanism by which SUMO-associated proteins – in this case, SUMO1-TRT – can be recruited to SIM sites on FOXM1. It is, however, not clear why the FOXM1mut construct should be more susceptible than the active FRET construct to such a process. One hypothesis is that SIM-mediated interactions occur more frequently when cells have been exposed to stresses; if impurities in the FOXM1mut-eGFP plasmid result in the transfection of this construct being more deleterious to cell health than transfection of the wild-type FOXM1 construct, this produce the observed higher baseline interaction. In summary, we have demonstrated the application of automated FLIM FRET to assay SUMOylation of FOXM1 and have observed similar dynamics compared to those established using biochemical assays. We note, however, the complexity of the interaction of FOXM1 with SUMO - particularly the presence of interaction sites (SIMs) other than those removed in the "non-SUMOylatable" FOXM15X(K>R) construct - makes the interpretation of FLIM-FRET results more challenging than for many other biological systems. We further note that for this particular assay it was critically important to establish a transfection protocol to reach an expression level that provides sufficient signal from the donor constructs without unduly compromising the living cells. Nevertheless, we believe that we have managed to produce a useful assay, taking advantage of the capabilities of the automated FLIM plate reader to provide statistically significant results in spite of the noise inherent in the biological signal through measurements of large numbers of cells. We also note the importance of the cell prefind algorithms that enable useful FLIM FRET data to be obtained from samples that do not express fluorophore constructs with high efficiency by identifying the small number of cells that are "useful" in terms of cell viability (evaluated through size and morphology), fluorescence intensity and donor-acceptor stoichiometry (evaluated by acquiring fluorescence images in multiple spectral channels).

Intramolecular FRET assay: Raichu biosensors at cell-cell junctions in keratinocytes

We have also explored the potential of our automated FLIM plate reader to readout FRET biosensors as a means of studying cell signalling processes. Such assays can be challenging because single molecule FRET biosensors frequently present relatively small changes in FRET efficiency between the open and close conformations. It has not proved possible to realise complete switching of a population of FRET biosensors[26,38]thus reducing the observable change in mean donor lifetime. Where FRET readouts correspond to small relative changes in lifetime (e.g. <10%), then the ability of automated plate readers to average readouts over 1000's of fields of view becomes critically important. Here we describe two preliminary investigations of signalling processes at adherens cell-cell junctions in keratinocytes using FRET biosensors to map the activation of two members of the Rho-family GTPases, RhoA and Rac1, utilising biosensor constructs derived from the "Raichu" (Ras and interacting protein chimeric unit) family of biosensors developed in the Matsuda laboratory[39]. The first study aimed to monitor RhoA activation in response to a "calcium switch" while the second study aimed to assay Rac1 activation modulated by CdGAP. Both studies were challenging in terms of achieving sufficient labelling density and in terms of reading out small donor lifetime changes. However, statistically significant results were achieved. Keratinocytes are epithelial cells that make up the vast majority of cells in the epidermis, providing structure and acting as a barrier between organisms and their environment. In physiological conditions, keratinocytes in layers are polarized, exhibiting different basal, lateral and apical domains. Junctions at lateral membranes between keratinocytes are required to maintain epithelial integrity under mechanical stresses but must also be dynamic in order that cells can respond properly during development, renewal and wound repair. Adherens junctions between keratinocytes fulfil crucial roles both mechanically, by providing a means for cells to form connections, and as foci for signalling events linked to cytoskeletal reorganisation. Dysregulation of adherens junctions is linked to epithelial tumour progression and metastasis[40], as well as to dermatological conditions such as pemphigus[41] and juvenile macular dystrophy[42,43].

Journal Name RSCPublishing

ARTICLE

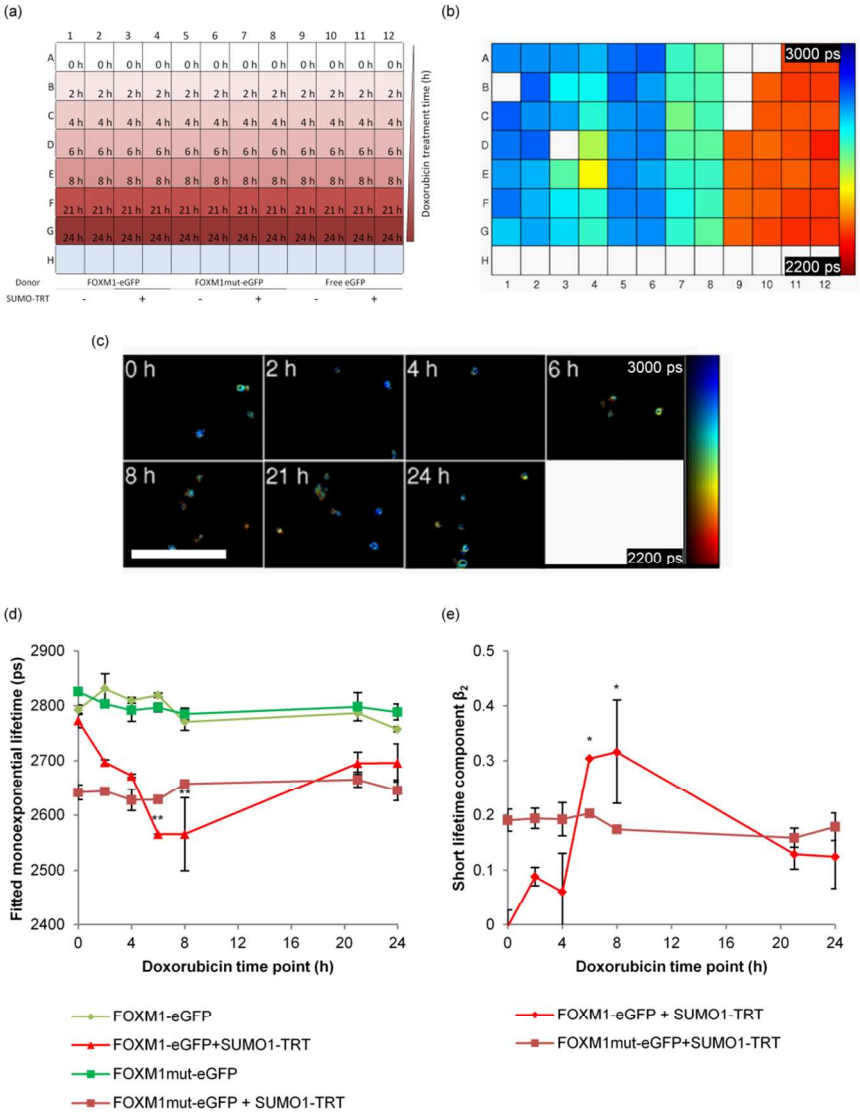

Fig. 5 Results of experiment investigating FOXM1 SUMOylation in response to a doxorubicin treatment time course: (a) Plate map showing layout of conditions in this experiment. (b) False colour plate map showing lifetime results of a monoexponential fit to data, averaged over fields of view per well. (c) Gallery image from FLIMfit illustrating heterogeneity of lifetimes within doses for cells expressing both FOXM1-eGFP and SUMO1-TRT constructs. Scale bar 200 µm. (d) Fitted monoexponential lifetimes plotted against doxorubicin treatment time. (e) Short lifetime contribution from a fitted biexponential model. Error bars represent standard errors over repeat wells; * indicates significance of difference from zero time point calculated using Dunnett's test.

Small GTPases (Ras superfamily GTPases) play key roles in a myriad of cellular signalling pathways, including those linked to control of cell morphology, motility and mitosis. Small GTPases function by hydrolysing guanosine triphosphate (GTP) to guanosine diphosphate (GDP); the terminal phosphate of GTP induces a conformational change of the small GTPase, rendering it active by allowing it to interact with its effectors. Conversely, when GTP is hydrolysed to GDP, interactions between the GTPase and its effectors are not possible, and the GTPase is considered inactive. Small GTPase activity is modulated by guanine-nucleotide exchange factors (GEFs) and GTPase activating proteins (GAPs). GEFs bind small GTPases and cause a conformational change that allows GDP to dissociate; free GTP may then bind the GTPase to activate it.

GAPs inactivate GTPase signalling by enhancing the hydrolysis of GTP to GDP. The interplay of GEFs and GAPs, which themselves are regulated by other proteins, allow fine tuning of GTPase signalling in the cell environment.

Ras homologous (Rho)-family of GTPases represents a branch of the Ras superfamily GTPases and 20 members of the Rho-family have been identified to date, with diverse cellular functions[44–46]. Aberrant expression and activity of Rho-family GTPases has been implicated in tumorigenesis and metastasis[44,46]. RhoA is one of the most extensively characterised proteins in the family, with multiple known effectors and regulators. Of interest here is its role in the assembly and stabilisation of cell-cell junctions[47,48] in epithelial cells. The activity of Rho-family GTPases can be modulated by cadherins ("calcium-dependent adhesion" proteins")[49], which are membrane-spanning proteins that can act as cell-cell receptors. Cadherins have been shown to undergo conformational changes upon calcium binding and calcium depletion is linked to a decrease in transjunctional interactions between cadherin dimers[50]. This behaviour has been described as the "calcium switch" for modulation of junction formation. Keratinocytes grown in low calcium conditions do not form cell-cell contacts but increasing calcium to physiological concentrations results in junction formation and epithelial polarisation, typically within 30 minutes of stimulation[51].

In the study reported here, we were interested to explore the activation of RhoA following stimulation of junction formation via the calcium switch since the Rho-family GTPases, and particularly RhoA, are implicated in regulation of assembly, remodelling and maturation of junctions[47]. For this we used the Raichu-RhoA biosensor[52,53], which shares the same basic design common to all of the Raichu probes, whereby activation of the small GTPase promotes binding to the corresponding binding domain. In the case of the Raichu-RhoA, the sensor region is human RhoA and the ligand region is the RhoA-binding domain of protein kinase N1 (PKN-RBD). When GTP binds to the RhoA region, the small GTPase is activated, allowing binding between the sensor and ligand domains. These binding events bring the donor and acceptor fluorophores into closer proximity, causing FRET to occur.

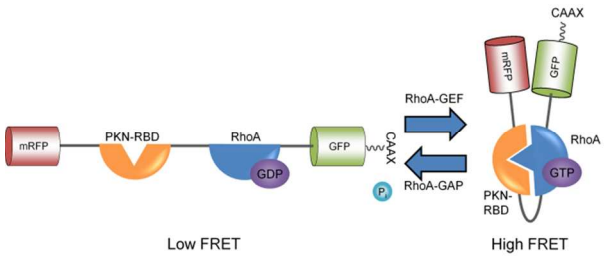

Fig. 6 Schematic of Raichu-RhoA FRET biosensor for RhoA activation mediated by RhoA-GEFs and RhoA-GAPs. PKN: protein kinase N1, CAAX: Ki-Ras4B CAAX motif allowing modification for membrane association, Pi: inorganic phosphate.

The RhoA-GEF proteins act to promote RhoA activity by liberating hydrolysed GDP from the probe, whilst RhoA-GAP proteins enhance the hydrolysis of the bound GTP, inactivating the probe: this behaviour is summarised in Fig. 6. In the probe used here, the native RhoA C-terminal CAAX (cysteine-aliphatic AA-aliphatic AA-any AA) region is replaced for a Ki-Ras4B CAAX motif, in order to promote delivery of the probe to plasma membrane rather than to intracellular membranes where endogenous RhoA is more often found. Since our experiments are concerned with RhoA activation at cell-cell junctions, this modification reduces background signal. The version of the probe gifted to our collaborators from the Ng lab (Richard Dimbleby Department of Cancer Research, King's College London, UK) has been modified from the original Raichu-RhoA sensor by replacing CFP and YFP with GFP and mRFP as the donor and acceptor fluorescent proteins, respectively[54]. To provide a negative control, a dominant negative form of the probe with a reduced affinity to guanine nucleotides was engineered by substitution of Thr for Asn at position 1237 (Raichu-RhoA T19N)[53]. To implement a positive control, cells were treated with FBS, which activates RhoA via growth factors contained in the serum. Fig. 7 shows the result of an assay of RhoA activation following stimulation of junction formation via the "calcium switch", which was implemented by adding calcium ions to a final concentration of 1.8 mM. Subsequently cells were fixed at different times following calcium switch and immunostained for E-Cadherin using Cy5. Fig. 7(a,b) show false colour lifetime maps of exemplar fields of view across calcium treatment time points, as well as from wells treated with serum as a positive control, for cells transfected with the dominant negative and wild-type Raichu-RhoA constructs respectively. Fig. 7(c,d) show the comparison between the mean "lateral membrane segmented" lifetimes resulting from a cell-wise fit to a monoexponential decay model averaged over untreated cells expressing the dominant negative form of the Raichu-RhoA probe (negative control) and serum treated cells transfected with wild-type Raichu-RhoA (positive control). The latter present a decrease in lifetime that is significant at $p < 0.05$ (Student's t-test), although we note that this corresponds to a mean lifetime change of only ~30 ps and that the Z' parameter associated these positive and negative controls would be Z' = -5.84, which by conventional criteria, would not furnish a useful assay for drug discovery. Fig. 7(e,f) show how the mean lifetime changes over time in response to the calcium switch for keratinocytes expressing the dominant negative and Raichu-RhoA constructs respectively. While there is no significant change in lifetime across the time course for the dominant negative construct; the active Raichu-RhoA probe presents a significant decrease in measured lifetime 60 minutes post-treatment ($p < 0.05$ compared to zero time point, Dunnett's test).

The same dataset was analysed with a different segmentation strategy to include the cytosol of each cell but exclude the lateral membrane region. As indicated in Fig. 8(a) the positive control condition (measured 5 minutes post serum stimulation) presented a significant decrease in mean lifetime compared to the negative control, indicative of RhoA being activated in the

cytosol. Furthermore, analysis with the same segmentation of the cytosol over the time course following the calcium switch resulted in Fig. 8(b), which indicates a transient decrease in donor lifetime at five minutes post-stimulation, although this change was not statistically significant ($p = 0.21$, Dunnett's test). At 60 minutes post calcium stimulation a statistically significant decrease in the mean lifetime was observed ($p < 0.05$, Dunnett's test). These results agree with a parallel biochemical study using Western blots to assay the amount of RhoA as a function of time after stimulation with calcium[48] where a transient increase in activated RhoA at 5 minutes post stimulation was observed. We note that this biochemical assay provided no spatial resolution and so would have been dominated by the signal from the cytosol.

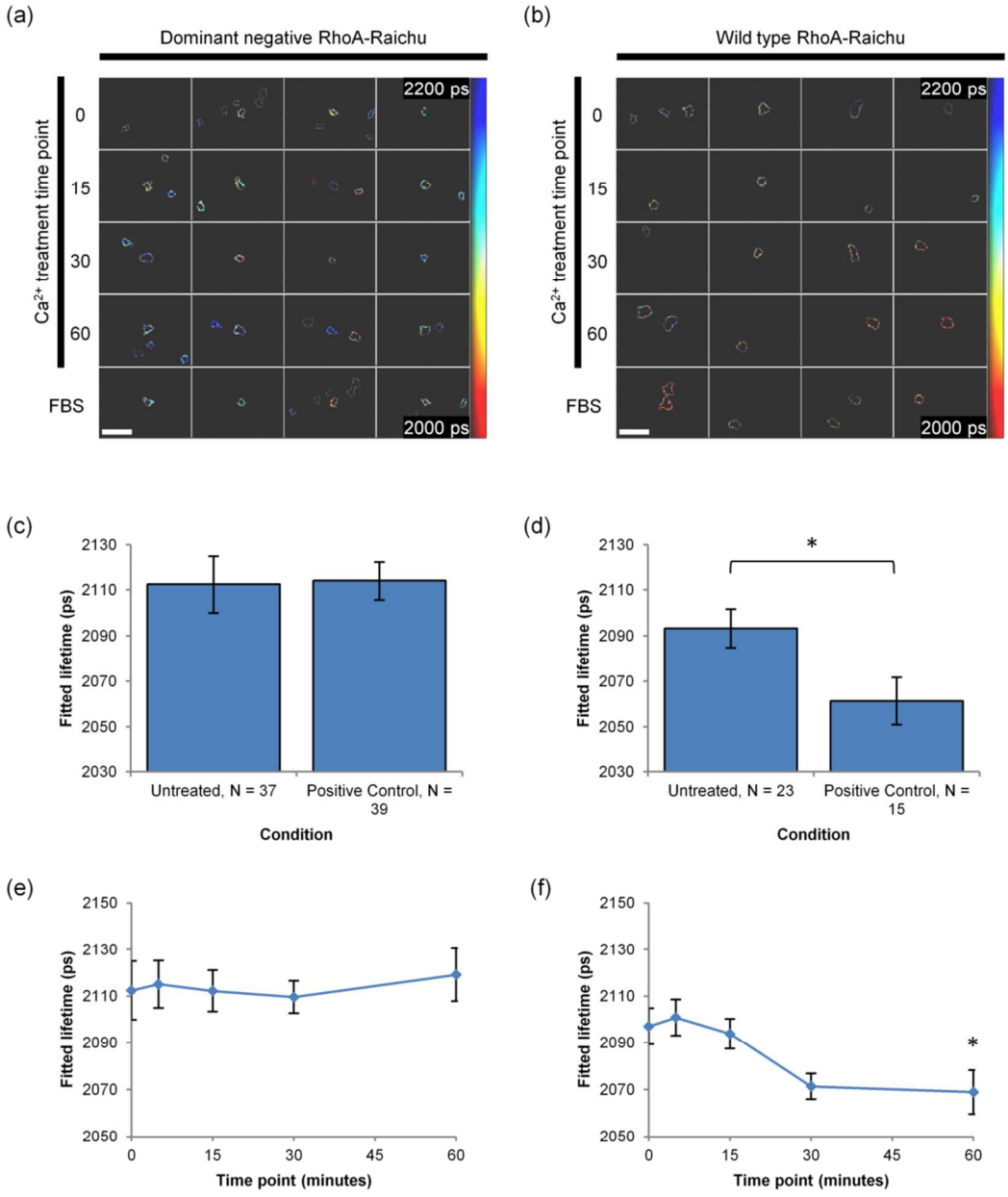

Fig. 7 RhoA activation in response to calcium switch: (a) False colour map showing monoexponential lifetime fit results following lateral membrane segmentation for typical fields of view in cells expressing the dominant negative form of Raichu-RhoA at different calcium treatment times, and 5 minute serum stimulation. (b) False colour map showing monoexponential lifetime fit results following lateral membrane segmentation for typical fields of view in cells expressing the wild-type form of Raichu-RhoA at different calcium treatment times, and 5 minute serum stimulation. Scale bar = 100 μm. (c) Monoexponential lifetimes averaged over cell lateral membranes to compare untreated and positive control (FBS) lifetimes for dominant negative Raichu-RhoA. (d) Monoexponential lifetimes averaged over cells to compare untreated and positive control (FBS) lifetimes for wild-type Raichu-RhoA ($p < 0.05$, Student's t-test). (e) Monoexponential lifetimes averaged over cell lateral membranes to show response to calcium switch treatment time course for dominant negative Raichu-RhoA. (f) Monoexponential lifetimes averaged over cell lateral membranes to show response to calcium switch treatment time course for wild-type Raichu-RhoA. Significance of difference from zero time point calculated using Dunnett's test.

Journal Name RSCPublishing

ARTICLE

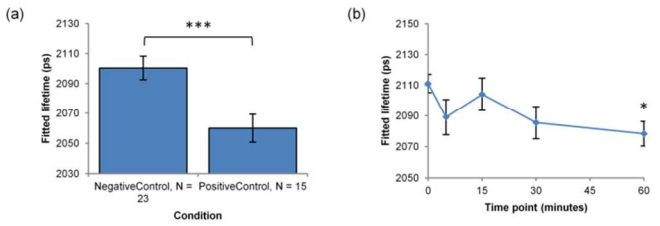

Fig. 8 Results of experiment investigating RhoA activation in response to calcium switch. (a) Monoexponential lifetimes averaged over cells (cytosol + lateral membrane) to compare untreated and positive control (FBS) lifetimes for wild-type Raichu-RhoA ($p < 0.005$, Student's t-test). (b) Monoexponential lifetimes averaged over cells (cytosol + lateral membrane) to show response to calcium switch treatment time course for wild-type Raichu-RhoA. Significance of difference from zero time point calculated using Dunnett's test.

In summary, the data presented in Fig. 7 and 8 shows that there is a statistically significant decrease in mean donor lifetime at the lateral membrane in keratinocytes transfected with the active Raichu-RhoA probe upon treatment with FBS and over 60 minutes following the calcium switch. A similar decrease in mean lifetime is also observed in the cytosol. Thus the Raichu-RhoA FRET probe may be used to assay RhoA activation at cell-cell junctions following the calcium switch although we note the donor lifetime changes are relatively low (<2%) and so great care should be taken to control systematic errors, with data being collected from a sufficiently large number of cells to average over random noise.

It was hoped that E-cadherin immunofluorescence staining could also be used to highlight cell-cell junction formation, thus providing both spatial and temporal context to the RhoA activation experiments in relation to junction formation. However, we did not obtain a useful signal from this staining in these experiments. We note that in earlier studies utilising Raichu FRET biosensors to investigate RhoA activation, ratiometric FRET measurements have yielded results indicative of much larger changes in mean FRET efficiency[55]. However, the biological systems were quite different; in particular, the earlier work used transfection of GAPs and GEFs to directly modulate RhoA activity. Although the lifetime differences we have measured here are small, we have previously demonstrated our wide-field time-gated FLIM instrument to be capable of resolving lifetime differences of less than 20 ps[6]; A key point to note is that the large number of measurements undertaken per condition in FLIM HCA experiments mitigates for both biological and instrumentation noise and enables such modest lifetime changes to be useful as readouts of FRET.

Intramolecular FRET assay: Rac1 small GTPase activation modulated by CdGAP

Rac1 is another Rho-family small GTPase, which is ubiquitously and constitutively expressed throughout mammalian tissue types. It is described as a pleiotropic gene, reflecting the diverse roles played by Rac1 in cells. These include a role in the regulation of cell-cell adherens junctions, where activated Rac1 has been shown to be critical in recruitment of actin at adhesive sites in the early stages of junction formation[56] and has further impact on junctions by regulating the endocytosis of E-cadherin[56–58].

More than 30 Rac1 effectors have been identified, associated with different cellular functions. In addition, a number of GEFs and GAPs that regulate the activity of Rac1, many of which have been found to play roles in adherens junction formation and maintenance[47] CdGAP is known to play important roles in cell spreading, migration and invasion, and more recently has been shown to be involved in the regulation of tight junctions following treatment with hepatocyte growth factor[59]. CdGAP has been identified by biochemical means as a GAP for Rac1[60,61]. In the study reported here, we explored the potential of a FLIM-FRET assay to probe the local regulation of Rac1 activity by CdGAP in the context of adherens junction formation in keratinocytes. This was also undertaken using a Raichu probe based on the Raichu-Rac construct originally developed in the Matsuda lab[53], for which the sensor region is Rac1 and the ligand region is the Cdc42/Rac interacting binding domain of the Rac1 effector PAK. As with Raichu-RhoA, a C-terminal Rac1 CAAX motif is included in the probe (gifted from the Ng lab, Richard Dimbleby Department of Cancer Research, King's College London, UK) utilised GFP and mRFP as donor and acceptor fluorophores[62], as illustrated in Fig. 9. CdGAP was expressed using the pRK5-myc vector and transfection of an empty pRK5-myc vector was used[63] as a negative control.

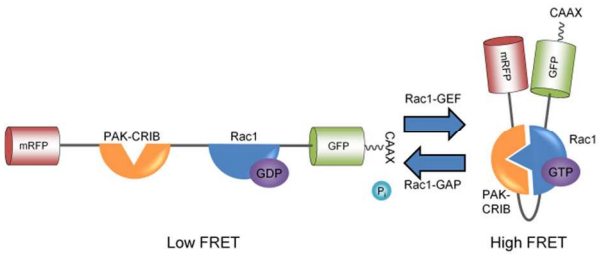

Fig. 9 Schematic of Raichu-Rac1 FRET biosensor for Rac1 activation mediated by Rac1-GEFs and Rac1-GAPs. PAK-CRIB: Cdc42/Rac interacting binding domain of P21 protein (Cdc42/Rac)-activated kinase 1, CAAX: Ki-Ras4B CAAX motif allowing modification for membrane association, Pi: inorganic phosphate.

Fig. 10(a-d) show the results of a monoexponential fit to manually segmented lifetime data with exemplar false colour maps showing fitted lifetime images of entire cells, with (lower 8 panels) and without (upper 8 panels) coexpression of CdGAP. The fitted lifetime data is presented by condition in Fig. 10(b), illustrating the significant increase ($p < 0.0001$, Student's t-test) in lifetime observed across the whole cell when CdGAP is overexpressed. False colour maps showing lifetime values in a 3-pixel wide region around the edge of segmented areas are shown in Fig.10(c), for which the lifetime data is summarised in Fig. 10(d). Again, there is a significant increase ($p < 0.0001$, Student's t-test) in fitted lifetime when CdGAP is overexpressed. Fig. 10(e, f) show lifetime data obtained using automated segmentation of whole cells for the same fields of view as those discussed above. This results in a greater number of "cell" regions being identified (for CdGAP overexpressing cells, N=61 compared to N=16 in the manual segmentation case), indicating the higher selectivity of manual segmentation by expert biologists. The false colour lifetime and lifetime histogram again indicate a significant increase in fitted lifetime in keratinocytes coexpressing CdGAP ($p < 0.0001$, Student's t-test).

Fig. 10(b, d, f) indicate a significant decrease in Rac1 activity in keratinocytes coexpressing CdGAP that is evident across all segmentation methods. This is in agreement with biochemical measurements[60] supporting the hypothesis that CdGAP reduces Rac1 activity. Comparing the negative controls (empty vector transfected cells) in Fig. 10(b, d), it is apparent that mean lifetimes averaged across lateral membranes are shorter than those averaged over whole cells, indicating that Rac1 is more likely to be active at the membrane than in the cytosol[64].

This experiment highlights the importance of image segmentation in the analysis. There was significant variation in keratinocyte size and shape within the set of cells deemed "acceptable" by manual quality control, which is difficult to accommodate using automated image segmentation. This challenge was compounded by the presence of fibroblasts that were co-cultured to increase the longevity and proliferation of keratinocytes and which expressed the fluorescent constructs at comparable levels to the keratinocytes. This may explain the differences observed between mean lifetimes obtained with manual and automated segmentation, i.e. comparing Fig. 10(b) and 10(f) where the average change in lifetime associated with manually segmented whole cells is approximately four times greater than that observed with automated segmentation, indicative of the inclusion of non-responding, unhealthy cells or sub-regions of bright fibroblasts by the automated segmentation algorithm. Accurate segmentation is especially critical when lateral membrane masks are generated since mis-segmented pixels make up a greater proportion of the regions of interest. For this study, where cells are cultured as a confluent monolayer, poor segmentation may erroneously include more of the cytosol - potentially decreasing the dynamic range of measurements of a probe that is primarily activated at the lateral membrane. For this reason it was decided that the automated segmentation algorithms currently available in *FLIMfit* could not satisfactorily segment lateral membrane regions of interest.

To summarise these studies of Raichu biosensors at adherens junctions in keratinocytes, we have demonstrated that quantitative lifetime-based readouts of the RhoA and Rac1 Raichu biosensors are possible although the lifetime changes are less than 2%. To achieve this accuracy, it is imperative to control for systematic errors including background fluorescence and to take the instrument response function (IRF) into account. We believe that these readouts would not be useable with the smaller numbers of cells that are practical to image with manual microscopy. The potential for of image segmentation to improve the analysis has been demonstrated. Future work could include optimisation of the E-cadherin and/or CdGAP labelling such that this could be used to define the segmentation of regions of interest corresponding to cell-cell junctions.

Methods

Automated FLIM HCA instrumentation

The automated fluorescence lifetime imaging plate reader is based on that described in references [13, 15] and is illustrated in Fig. 11. It utilises an Olympus IX81 frame with motorised dichroic cassette, objective turret and stage as well as the Olympus ZDC focus drive unit to allow automatic focusing. A motorised sample stage (Märzhauser Wetzlar GmbH, Scan Im) allows for software controlled sample movement, enabling whole plates (96-well, 384-well) to be imaged automatically. The instrument is controlled using custom software written in LabView (National Instruments). This allows the user to set up fully automatic and unsupervised FLIM acquisitions.

Excitation is provided by a fibre-laser pumped supercontinuum source (Fianium UK Ltd, SC 400-6) providing ~6 ps pulses at 60 MHz repetition rate with 1.5-5 mW/nm output over visible wavelengths (400-700 nm). A motorised filter wheel was used to select the excitation wavelength and the average excitation power was monitored using a photodiode read to the acquisition PC using a DAQ card. The excitation light was then conveyed to the illumination port using an optical fibre. When shorter excitation wavelengths are required, a frequency-doubled femtosecond Ti:Sapphire laser (Newport Spectra Physics, Mai-Tai) providing ~100 fs pulses at 80 MHz could be utilised. For wide-field FLIM, the excitation was coupled into the microscope through the illumination port via a rotating diffuser placed in the light path between the end of the delivery fibre and the fluorescence illuminator (IX2-RFA, Olympus) in the back port of the IX81 microscope frame. A dual lamp house adapter (U-DULHA, Olympus) was included in the illumination path to allow switching between a mercury lamp and the pulsed laser source. For optically sectioned imaging a Nipkow disk unit (Yokogawa, CSU-X) was utilised as illustrated in Fig. 3(b). In this configuration, a single mode-polarising preserving optical fibre delivered the excitation light directly to the CSU-X unit. Fluorescence is detected using a gated optical intensifier (Kentech Instruments; model HRI) read

out by a cooled CCD (Hamamatsu Photonics; model Orca ER II). Fluorescence decays are sampled using 6 to 8 time-gates a delays spaced evenly throughout the decay profile that are typically greater than 1 ns in duration but with rising edges of ~50 ps. Unless stated otherwise, images were acquired using a 40x long working distance air objective (Olympus, LUCPLFLN 40) with an NA of 0.6.

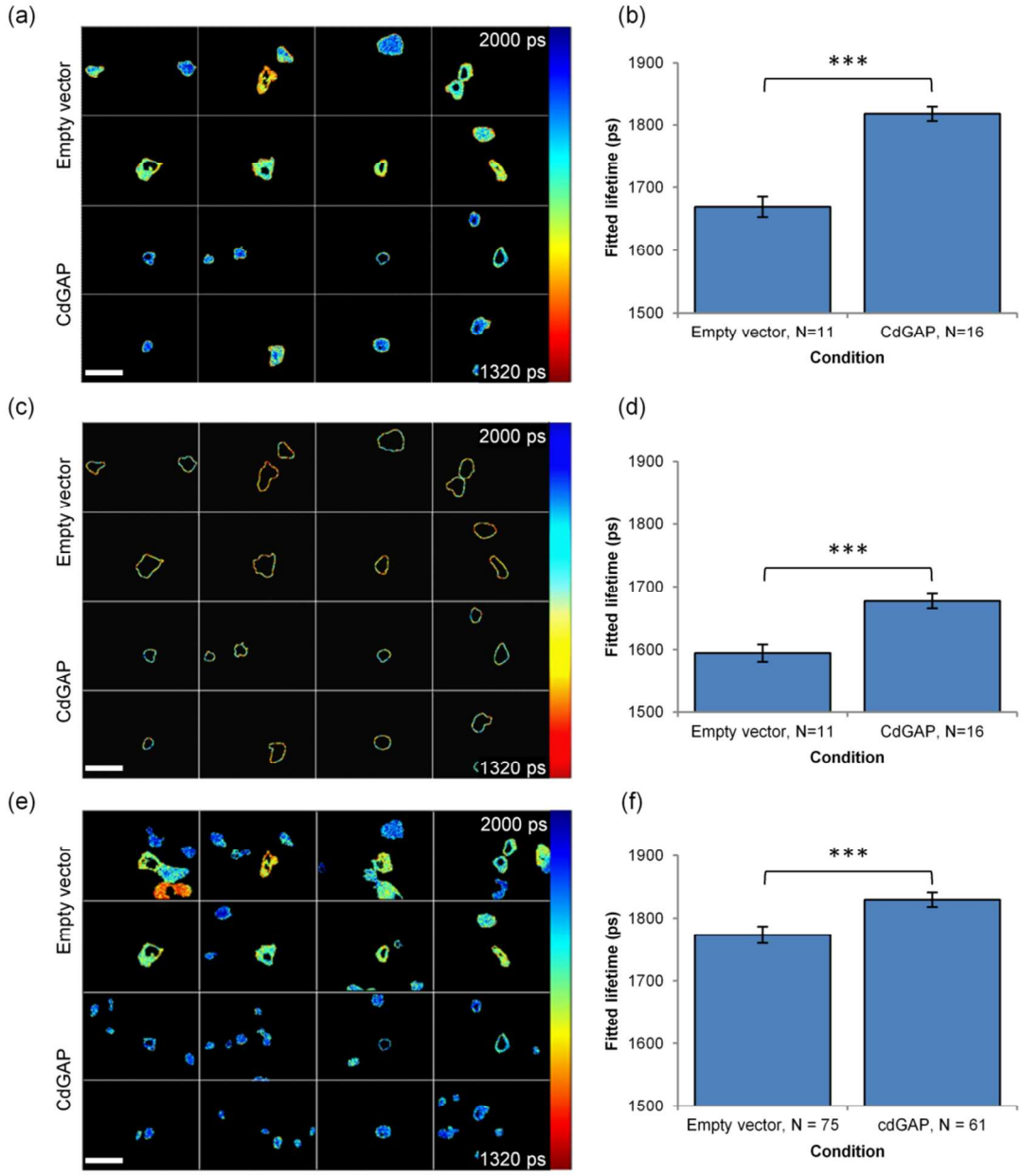

Fig. 10 Rac1 activation mediated by CdGAP: (a) false colour plots showing monoexponential lifetime fit results for typical fields of view in cells with and without overexpression of CdGAP, whole cell analysis following manual segmentation. (b) Bar chart of monoexponential lifetimes averaged over N manually segmented cells per condition. Error bars show standard errors calculated over N cells per condition. Significance of difference $p < 0.0001$, Student's T-test. (c) False colour plots showing monoexponential lifetime fit results for typical fields of view in cells with and without overexpression of CdGAP, "lateral membrane-only" analysis following manual segmentation. (d) Bar chart of monoexponential lifetimes averaged over N manually segmented cell membranes per condition. Significance of difference $p < 0.0001$, Student's T-test. (e) False colour plots showing monoexponential lifetime fit results for typical fields of view in cells with and without overexpression of CdGAP following automated segmentation. (f) Bar chart of monoexponential lifetimes averaged over N manually segmented cells per condition. Error bars show standard errors calculated over N cells per condition. Significance of difference $p < 0.0001$, Student's T-test. Scale bars = 100 µm.

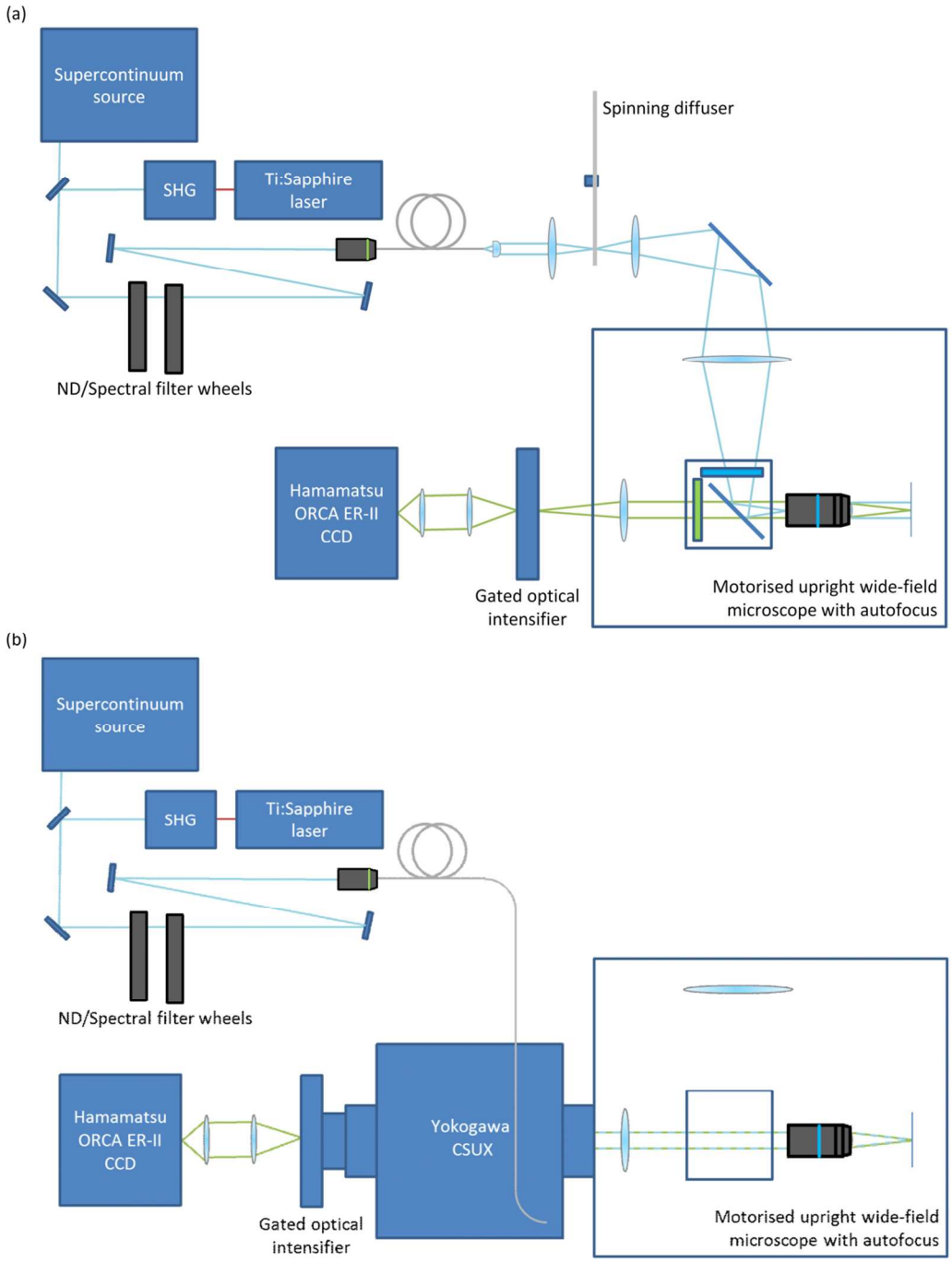

Fig. 11 (a) automated wide-field FLIM plate reader and (b) automated optically sectioning FLIM plate reader.

Prior to FLIM acquisition, the plate reader can be set to perform an automatic cell finding ("pre-find") scan to rapidly identify and map FOV containing suitable cells for the FLIM assay. This is a particularly useful step for sparsely labelled samples. A number of pre-find routines are available, typically either spiralling out from the centre of the well or seeking around the edge of the well with programmable pattern recognition to identify a user-specified numbers of "cells. The instrument provides the option of using a lower magnification objective for increased prefind speed and performing a pre-find in two spectral channels to ensure that only cells expressing both donor and acceptor plasmids to an acceptable level are imaged. Typically the prefind process takes ~30 minutes to find 4 FOV in each of 96 wells.

As part of each FLIM acquisition, the background fluorescence level is measured, typically using wells containing unlabelled cells prepared under the same conditions as the experiment. It is also usual to include some wells containing a reference

fluorophore that can be used to measure the time delay of the IRF or to provide a reference decay when fitting with reference reconvolution[65]. The IRF can be measured using a short lifetime reference fluorophore or by detecting scattered excitation light. Data is analysed using *FLIMfit*[17,] which can account for contributions from a constant background of stray light, scattered excitation light and a time-varying noise background, providing that appropriate background measurements are made. The effect of incomplete fluorescence decay profiles from previous excitation pulses are included in the model and global analysis techniques can be applied to fit to complex decay models. *FLIMfit* can also incorporate image segmentation to define regions of interest, such as cells, cell membrane regions, cytoplasm, nucleus etc., across which pixels can be binned for direct fitting or across which global fitting can be undertaken.

A choice of segmentation algorithms is presented to the user in the Segmentation Manager tool in *FLIMfit*. Of these, the algorithm used in for the data presented here is based on a size-tuned non-linear top hat function described previously[15]. Briefly, this method transforms images pixelwise, enhancing the brightness of a pixel if its close vicinity is also bright and its distant vicinity (local background) is dim, where the scale of features and local background are user defined quantities. A binary image is generated from the transformed image by applying a user-defined threshold, the resultant binary image is smoothed using standard MATLAB functions and spatially distinct regions are identified. These regions are then size-sieved to remove objects smaller than a user-defined threshold, such as cell debris. If lateral membrane segmentation is desired, segmentation masks are subjected to an erode operation and the resulting binary image is subtracted from the original mask. In addition, the Segmentation Manager can be used to import TIFF images generated externally, for example by the *CellSegmenter* program described below, to use as segmentation masks in *FLIMfit*.

HIV-1 Gag protein oligomerisation assay

The automated optically sectioning FLIM microscope configuration was employed for this work using the supercontinuum source to excite the CFP donor. A key consideration for live cell assays is the cell culture medium, which is needed to maintain a healthy cell population during the course of the experiment but which should contribute as small a background fluorescence as possible in the detection window for CFP defined by the emission filter (483/35 nm). Different preparations of DMEM were compared in terms of their contribution to the background fluorescence and the best results were obtained for DMEM without FCS but with phenol red, which presented a background approximately 7% of the typical CFP signal. All work was carried out using HeLa cells maintained in DMEM (Gibco), 2.5%antibiotic/antimycotic and 2.5% L-glutamine. Cells were maintained at 37°C, 5%CO2 and grown until 80-90% confluent in T75 flasks (Corning) before passaging using trypsin to detach the cells.

Prior to transfection, cells were transferred from growth media, washed in phosphate buffered saline (PBS) and placed in Optimem I reduced serum media (Gibco).Transfections were performed using Lipofectamine 2000 (Invitrogen). Transfection mixes were prepared following manufacturers' instructions using a total of 150 ng of plasmid DNA per well with a 2:1 ratio of lipids to DNA. The transfection mixes were left on the cells for 6 hours and then washed in PBS and the media replaced with growth media. The addition of NMT inhibitor doses was performed at the same time as the lipofection, with the NMT inhibitor being diluted into the Optimem I used to seed the cells prior to transfection.

For the live cell measurements, an environmental chamber (Solent Scientific) was utilised to enable the live cell assay to be conducted at 37° and buffered at 5% CO_2 - the conditions used when culturing and transfecting the cells. Maintaining the 5% CO_2 atmosphere is important to minimise changes in pH, which can alter the fluorescence properties of fluorescent proteins[66]. The environmental chamber was allowed to equilibrate to 37°C for 24 hours prior to imaging to ensure that a stable temperature was achieved and cells were placed into the environmental chamber 30 minutes prior to measurements being made, to allow a stable temperature to be reached. Typically, most of this time was used to set up the acquisition and perform the pre-find routine.

Assay of SUMOylation of FOXM1 protein

MCF7 cells were seeded at a density of 10^4 per well on Greiner μClear plates in standard growth media. Particular care was taken to ensure a single cell suspension, and the plate was tilted vigorously to ensure that cells were distributed evenly within wells. The sample was incubated for 24 h at 37°C. Based on results from experiments in the preceding section, transfections were carried out using XtremeGene HP according to the manufacturer's instructions with a transfection reagent:plasmid ratio of 2:1 (volume:weight). Donor constructs (FOXM1-eGFP, negative control FOXM1mut-eGFP or free eGFP) were transfected at 0.1 μg per well; SUMO1-TRT was transfected at 0.025 μg per well.

SUMO1-TRT is adapted from a fluorescent protein tagged SUMO1 construct gifted from the Ng lab (Richard Dimbleby Department of Cancer Research, King's College London, UK) using a TagRFP-T fluorescent protein gifted by Alex Sardini (Cellular Stress group, MRC Clinical Sciences Centre, Imperial College London).

The layout of donor-only and cotransfected wells within the plate is shown in Fig. 5(a-b). Cells were incubated with transfection mixtures for 24 h, after which media was replaced. Wells designated for 24 h treatment were treated at this point with 0.1 μM doxorubicin, freshly diluted in growth media from stock (3400 mM). 3 hours later (21 hours prior to end point), media in all wells was again replaced; this time, media supplemented with doxorubicin was used for both 24 h and 21 h treatment wells. This process was repeated for 8 h, 6 h, 4 h and 2 h treatment wells (16 h, 18 h, 20 h and 22 h after starting treatment, respectively). The layout of doxorubicin-treated

wells is illustrated in Fig. 5(a). Two hours after the final treatment was administered, all media was removed and replaced with glucose-supplemented HBSS at 37°C. The sample was then transferred to the microscope incubator.

To identify fields of view that were sufficiently populated with cells expressing the donor constructs, a coverage-based prefind scan was undertaken using a 40x long working distance objective (LUCPlanFLN 40x/0.6) and Hg lamp illumination through the GFP filter cube (excitation: 472/30 nm, dichroic: 495 nm, emission: 520/35 nm). NTH segmentation was applied to integrated donor intensity images to identify objects ("cells") of sufficient size, intensity and signal to background ratio. In addition, for wells in which acceptor constructs were cotransfected, an additional constraint was imposed such that the minimum level of acceptor upper quartile per segmented region should be 500 DN in order to exclude cells with low expression of SUMO1-TRT from analysis. For the data analysis, a time-varying background decay was measured from a well of untransfected cells using the same acquisition parameters as the automated experiment, and a reference decay profile was obtained from a well containing 25 μM Erythrosine B.

The prescan was set to identify four fields of view per well and then automated FLIM data was acquired using the same long working distance 40x objective in the same spectral channel across 7 time gates of 3 ns duration, for each of which the camera was exposed for 0.8 s. As well as FLIM of the donor, intensity images of the SUMO1-TRT were acquired in the spectral channel defined by the "red" filter cube (excitation: 545/30 nm, dichroic: 570 nm, emission: 610/75 nm); a single exposure of 0.02 s was acquired at a single time delay chosen to lie at the peak of the donor decay profile. In total, the automated acquisition of 384 fields of view took 72 minutes.

Intramolecular FRET assay: RhoA Raichu biosensor

Human keratinocytes isolated from neonatal foreskin (strain SF, passages 3-6) were maintained on mitomycin-C (Sigma, Dorset, UK) treated J2 mouse fibroblasts in standard medium (Dulbecco's Modified Eagle Medium (DMEM) DMEM:F12 BioWittaker, Lonza, Germany) supplemented with 1.8mM CaCl2, 10% foetal calf serum (FCS), 5mM glutamine, 100 units/ml penicillin, 100μg/ml streptomycin, 5μg/ml insulin, 10ng/ml epidermal growth factor (EGF), 0.5μg/ml hydrocortisone (all Sigma) and 0.1nM cholera toxin (Quadratech Diagnostics Ltd, Surrey, UK) as described elsewhere240–243. Low calcium medium (approximately 0.1mM CaCl2) had the same formulation as standard medium but contained FCS pre-treated with Chelex-100 resin (BioRad, Hemel Hempstead, UK) to deplete divalent calcium ions[67]. Cells to be grown in low calcium were seeded in standard medium and switched to low calcium when approximately 20 cells per colony were seen. Cells were seeded on 96 well plates (Corning Incorporated, Corning, NY) at a density of 2.2×10^3 cells per well. Cells were maintained at 37°C, 5% CO^2. J2 mouse fibroblasts were maintained in medium consisting of Dulbecco's modified medium (DMEM, Sigma-Aldrich), 10% DCS (Sera Laboratories International Ltd, West Sussex, UK) and 5mM L-glutamine (Sigma-Aldrich).

Transfections were performed using plasmid DNA diluted in Effectene buffer (Qiagen) and Enhancer added at a ratio of 1:8 Enhancer. 0.05 μg/well DNA plasmid encoding the EGFP-mRFP-modified version of the Raichu 1240[55] construct illustrated in Fig. 6 was used per well. Control wells were transfected using a plasmid encoding a dominant negative form of the probe subject to a single point mutation (T19N) that cannot be activated and therefore remains always in the low FRET conformation. Samples were vortexed and incubated for 5 minutes at room temperature. Effectene transfection reagent was added at a ratio of 1:25 Effectene and tubes vortexed prior to 5 minutes' incubation at room temperature. Low calcium medium was used to dilute the final plasmid DNA mixture which was subsequently added to cells. Media was changed after 4 hours.

The calcium switch was implemented by adding calcium ions to a final concentration of 1.8 mM[48]. At different times following induction of junction formation by the calcium switch, cells were fixed with 3% paraformaldehyde (PFA) in phosphate-buffered saline (PBS) for 10 minutes at room temperature (RT) then washed 3 times in PBS. Immunofluorescence labelling was then undertaken to investigate E-cadherin translocation upon cell-cell junction formation. Cells were simultaneously permeablised and blocked with 0.1% Triton X-100 (Sigma-Aldrich) diluted in 10% FCS-PBS solution, for 10 minutes at RT. Cells were then washed 3 times in PBS before staining. Samples were incubated with primary antibody against E-cadherin (mouse, gifted by M. Takeichi (NCCRI, Tokyo, Japan)) diluted in 10% FCS (final concentration) in PBS for 30 minutes in the dark at RT. Samples were washed nine times in PBS before incubation for 30 minutes in the dark at RT with secondary antibody (Cy5-conjugated anti-mouse (Jackson Immuno labs)). Cells were washed a further nine times in PBS then 3 times in water before addition of Mowiol mounting media. Samples were imaged at room temperature.

Cells expressing Raichu-RhoA were found using the prefind algorithm with 10x magnification under mercury lamp illumination via the GFP filter set. After optimisation of transfection, intensity thresholding was sufficient to identify cells expressing the probe. Imaging was carried out at 40x magnification (LUCPFLN 40x, Olympus). FLIM data was acquired in the GFP spectral channel across six time gates acquired with integration times of 1.2 seconds. A similar exposure was acquired with Cy5 filters at a single time delay close to the maximum of the fluorescence signal in order to assess E-cadherin localisation and phase contrast images were acquired in order that cells could be verified to have grown in a monolayer. 360 fields of view were acquired across 60 wells, leading to a total acquisition time of 84 minutes. A well seeded with untransfected keratinocytes was imaged using the same acquisition parameters as the FLIM experiments in order to measure the time-varying fluorescent background and a well of

20 μM Erythrosine was imaged to provide a reference decay profile.

For the data analysis, image segmentation was undertaken manually since the significant variation of size and shape of acceptable cells and the presence of bright fibroblasts was found to confound the automatic segmentation algorithms at our disposal. Manual cell segmentation was realised using a custom segmentation program ("*CellSegmenter*") written in Java for Android to allow segmentation to be performed by drawing around cells with a finger or stylus on a tablet or mobile phone, with standard swipe and pinch gestures being used to pan and zoom the image. This enabled segmentation of cytosol and lateral membrane regions of interest and also enabled unhealthy cells to be rejected from the analysis. Once the cell outlines had been established, the lateral membrane region was defined to be 6 pixels wide and was formed using an erode operation followed by a subtraction in MATLAB. Then "cytosol" masks were generated in MATLAB by combining whole cell and lateral membrane masks in a NAND operation. Segmented data was fitted pixel-wise to a monoexponential lifetime model in *FLIMfit* using the measured reference decay profile and time varying background. Mean lifetimes and standard errors were calculated cell-wise and presented by condition.

Intramolecular FRET assays: Rac1 Raichu biosensor

Cells were cultured as outlined in the previous section. Transfections were performed using plasmid DNA diluted in Effectene buffer (Qiagen) and Enhancer added at a ratio of 1:8 Enhancer. Samples were vortexed and incubated for 5 minutes at room temperature. Effectene transfection reagent was added at a ratio of 1:25 Effectene and tubes vortexed prior to 5 minutes' incubation at room temperature. Standard medium was used to dilute the final plasmid DNA mixture which was subsequently added to cells. Media was changed after 4 hours. A variety of transfection conditions were tried in order to optimise expression level and cell viability and the optimum was found to be 0.05 μg/well Raichu plasmid, 0.2 μg/well CdGAP or empty vector plasmid.

In order that CdGAP levels could be assayed, cells were permeablised using 0.1% Triton X-100 in 10% FCS for 10 minutes at room temperature following fixation with 3% PFA (10 minutes, room temperature). Samples were incubated with primary and secondary antibodies (myc A14 (rabbit, Santa Cruz) and anti-rabbit Cy5 (Jackson Immuno labs)) in 10% FCS-PBS sequentially for 30-60 minutes, followed by nine washes in PBS and three washes in water after each incubation. Each well of the 96-well plates was covered with 150 μl Mowiol before imaging at room temperature.

It was found that the majority of cells presenting Cy5 fluorescence also presented GFP (Raichu donor) signal. On this basis, the low magnification cell prefind step was performed only in the Cy5 channel to increase speed, reduce photodamage to cells and to reduce photobleaching of the FLIM donor. Imaging was then carried out at 40x magnification (LUCPFLN 40x, Olympus). FLIM data was acquired in the GFP spectral channel (excitation: 472/30 nm, dichroic: 495 nm, emission: 520/35 nm) with 0.5 s integration at six time gates. A single 0.5 s integration time snapshot per field of view was acquired at the peak of the fluorescence decay using Cy5 filters (excitation: 620/60 nm, dichroic: 660 nm, emission: 700/75 nm) in order that expression of CdGAP could be assessed. Phase contrast images were also taken at each field of view. 325 fields of view were acquired across 36 wells, leading to a final acquisition time of 70 minutes. A well seeded with untransfected keratinocytes was imaged using the same acquisition parameters as the FLIM experiment to measure the time-varying fluorescent background and a well of 20 μM Erythrosine was imaged to provide a reference decay profile.

Analysis of this dataset was undertaken using both manual and automated image segmentation. For manual segmentation, the *CellSegmenter* Android app (see previous section) was used to outline cells in GFP intensity images (obtained by integrating FLIM data) and cells not presenting Cy5 fluorescence were rejected from analysis. "Lateral membrane" masks were generated from the manually segmented cell masks by erosion and subtraction with membrane width parameter set to 3 pixels. When automated cell segmentation was used, the GFP intensity images were outlined using the NTH algorithms implemented in *FLIMfit* and then the procedure was repeated using the Cy5 intensity images. A MATLAB script was used to reject any cells in the acquired fields of view that did not exhibit both GFP and myc-Cy5 signal by a pixelwise AND operation followed by size thresholding.

Conclusions

In conclusion, we have demonstrated that an automated FLIM plate reader can be applied to systematically study protein interactions and to read out FRET biosensors in fixed and live cells at rates of ~ 10 seconds per field of view. The use of global fitting techniques permits even complex decay models to be fitted with modest photon numbers compatible with live cell imaging. By analysing readouts of 100's of FOV, it is possible to obtain statistically significant results with readouts based on lifetime changes of 10's of picoseconds (corresponding to only a few% change in lifetime). Some of the exemplar biological studies reported here have been particularly challenging and perhaps represent the limit of performance that may be reasonably expected once sources of systematic error have been eliminated. Throughout this work our appreciation of the importance of appropriate biological controls has been strengthened. With improved fluorescent labels that are bright and present monoexponential decays, we believe that assay performance and speed can be improved well beyond what we have presented here. We note that FRET measurements utilising fluorescent proteins should always be treated with caution, particularly considering the assumptions regarding the relative orientation of donor and acceptor dipoles[68] Nevertheless, as indicated here and in prior work, automated FLIM of FRET readouts can realise useful assays to provide information that is significantly more robust than what is

achievable with manual microscopy. To further the opportunities for automated FLIM to be used by the wider community, we are working to adapt the instrument described here to open source acquisition and control software based on the μManager software platform[69].

Acknowledgements

The authors gratefully acknowledge funding from the UK Biotechnology and Biological Sciences Research Council (BBSRC BB/E003621/1 and BB/H00713X/1), the UK Engineering and Physical Sciences Research Council (EPSRC Pathways to Impact grant), the Wellcome Trust (WT 095931/Z/11/Z) and the UK Technology Strategy Board (Technology Award CHBT/007/00030, EP/C54269X, in partnership with AstraZeneca, GE Healthcare, GSK, Kentech Instruments Ltd). DA, DK and SW acknowledge PhD studentships from the Institute of Chemical Biology EPSRC funded Doctoral Training Centre. N.W. and J.M acknowledge BBSRC Doctoral Training studentships (BB/D526410/1) EWT thanks the BBSRC (David Phillips Research Fellowship to EWT, grant BB/D02014X/1). ET thanks CR-UK for a research studentship grant (C29637/A10711), and RS thanks the EU for the award of an Intra-European Fellowship (PIEF-GA-2010-273868).

Notes and references

[a] Photonics Group, Department of Physics, Imperial College London.
[b] Institute for Chemical Biology, Department of Chemistry, Imperial College London.
[c] National Heart and Lung Institute, Faculty of Medicine, Imperial College London. Sir Alexander Fleming Building, London SW7 2AZ, UK.
[d] Chemical Biology Section, Department of Chemistry, Imperial College London, SW7 2AZ.
[e] Department of Surgery and Cancer, Imperial College London, Du Cane Road, London, W12 0NN, UK.
[f] Retroscreen Virology Ltd, London EC1 2AX.
[g] Pfizer Global Research and Development, Pfizer Limited, Sandwich, Kent.
[h] Centre for Histopathology, Imperial College London, Du Cane Road, London, W12 0NN, UK.

1 E. A. Jares-Erijman and T. M. Jovin, *Curr. Opin. Chem. Biol.*, 2006, **10**, 409–16.
2 C. M. Welch, H. Elliott, G. Danuser and K. M. Hahn, *Nat. Rev. Mol. Cell Biol.*, 2011, **12**, 749–56.
3 R. M. Clegg, in *Laboratory Techniques in Biochemistry and Molecular Biology*, ed. T. W. J. Gadella, Elsevier, 2009, vol. 33, pp. 1–57.
4 A. Hoppe, K. Christensen and J. A. Swanson, *Biophys. J.*, 2002, **83**, 3652–64.
5 P. H. Bastiaens and A. Squire, *Trends Cell Biol.*, 1999, **9**, 48–52.
6 S. Kumar, D. Alibhai, A. Margineanu, R. Laine, G. Kennedy, J. McGinty, S. Warren, D. J. Kelly, Y. Alexandrov, I. Munro, C. Talbot, D. W. Stuckey, C. Kimberly, B. Viellerobe, F. Lacombe, E. W.-F. Lam, H. Taylor, M. J. Dallman, G. Stamp, E. J. Murray, F. Stuhmeier, A. Sardini, M. Katan, D. S. Elson, M. A. A. Neil, C. Dunsby and P. M. W. French, *Chemphyschem*, 2011, **12**, 609–26.
7 P. B. Jones, L. Herl, O. Berezovska, A. T. N. Kumar, B. J. Bacskai and B. T. Hyman, *J. Biomed. Opt.*, 2006, **11**, 054024.
8 D. R. Matthews, S. M. Ameer-Beg, P. Barber, G. P. Pierce, R. G. Newman, B. Vojnovic, L. M. Carlin, M. D. Keppler, T. Ng, K. Suhling and M. Irving, in *Biomedical Optics (BiOS) 2008*, eds. D. L. Farkas, D. V. Nicolau and R. C. Leif, International Society for Optics and Photonics, 2008, pp. 685919–685919–12.
9 D. M. Grant, J. McGinty, E. J. McGhee, T. D. Bunney, D. M. Owen, C. B. Talbot, W. Zhang, S. Kumar, I. Munro, P. M. P. Lanigan, G. T. Kennedy, C. Dunsby, A. I. Magee, P. Courtney, M. Katan, M. A. A. Neil and P. M. W. French, *Opt. Express*, 2007, **15**, 15656–15673.
10 J. R. Lakowicz, H. Szmacinski, K. Nowaczyk, K. W. Berndt and M. Johnson, *Anal. Biochem.*, 1992, **202**, 316–330.
11 A. Esposito, T. Oggier, H. C. Gerritsen, F. Lustenberger and F. S. Wouters, *Opt. Express*, 2005, **13**, 9812.
12 A. Esposito, C. P. Dohm, M. Ba and F. S. Wouters, *Mol. Cell. Proteomics*, 2007, **6**, 1446–1454.
13 C. B. Talbot, J. McGinty, D. M. Grant, E. J. McGhee, D. M. Owen, W. Zhang, T. D. Bunney, I. Munro, B. Isherwood, R. Eagle, A. Hargreaves, M. Katan, C. Dunsby, M. A. A. Neil and P. M. W. French, *J. Biophotonics*, 2008, **1**, 514–521.
14 H. E. Grecco, P. Roda-Navarro, A. Girod, J. Hou, T. Frahm, D. C. Truxius, R. Pepperkok, A. Squire and P. I. H. Bastiaens, *Nat. Methods*, 2010, **7**, 467–72.
15 D. Alibhai, D. J. Kelly, S. Warren, S. Kumar, A. Margineau, R. A. Serwa, E. Thinon, Y. Alexandrov, E. J. Murray, F. Stuhmeier, E. W. Tate, M. A. A. Neil, C. Dunsby and P. M. W. French, *J. Biophotonics*, 2013, **6**, 398–408.
16 S. Pelet, M. J. R. Previte, L. H. Laiho and P. T. C. So, *Biophys. J.*, 2004, **87**, 2807–17.
17 S. C. Warren, A. Margineanu, D. Alibhai, D. J. Kelly, C. Talbot, Y. Alexandrov, I. Munro, M. Katan, C. Dunsby and P. M. W. French, *PLoS One*, 2013, **8**, e70687.
18 A. Ono, *Future Virol.*, 2009, **4**, 241–257.
19 O. W. Lindwasser and M. D. Resh, *Proc. Natl. Acad. Sci. U. S. A.*, 2002, **99**, 13037–42.
20 V. Goncalves, J. A. Brannigan, E. Thinon, T. O. Olaleye, R. Serwa, S. Lanzarone, A. J. Wilkinson, E. W. Tate and R. J. Leatherbarrow, *Anal. Biochem.*, 2012, **421**, 342–4.
21 M. A. Rizzo, G. H. Springer, B. Granada and D. W. Piston, *Nat. Biotechnol.*, 2004, **22**, 445–9.
22 S. V Koushik and S. S. Vogel, *J. Biomed. Opt.*, 2008, **13**, 031204.
23 D. Alibhai, PhD Thesis, Imperial College London, 2013.
24 E. Thinon, R. A. Serwa, M. Broncel, J. A. Brannigan, U. Brassat, M. H. Wright, W. P. Heal, A. J. Wilkinson, D. J. Mann and E. W. Tate, *Nat. Commun.*, 2014, **5**, 4919.
25 A. Villoing, M. Ridhoir, B. Cinquin, M. Erard, L. Alvarez, G. Vallverdu, P. Pernot, R. Grailhe, F. Mérola and H. Pasquier, *Biochemistry*, 2008, **47**, 12483–92.
26 R. Laine, D. W. Stuckey, H. Manning, S. C. Warren, G. Kennedy, D. Carling, C. Dunsby, A. Sardini and P. M. W. French, *PLoS One*, 2012, **7**, e49200.

27 S. H. Giordano, Y.-L. Lin, Y. F. Kuo, G. N. Hortobagyi and J. S. Goodwin, *J. Clin. Oncol.*, 2012, **30**, 2232–9.
28 J. Laoukili, M. R. H. Kooistra, A. Brás, J. Kauw, R. M. Kerkhoven, A. Morrison, H. Clevers and R. H. Medema, *Nat. Cell Biol.*, 2005, **7**, 126–36.
29 P. Raychaudhuri and H. J. Park, *Cancer Res.*, 2011, **71**, 4329–33.
30 C.-Y. Koo, K. W. Muir and E. W.-F. Lam, *Biochim. Biophys. Acta*, 2012, **1819**, 28–37.
31 J. Millour, N. de Olano, Y. Horimoto, L. J. Monteiro, J. K. Langer, R. Aligue, N. Hajji and E. W. F. Lam, *Mol. Cancer Ther.*, 2011, **10**, 1046–58.
32 Y. Tan, P. Raychaudhuri and R. H. Costa, *Mol. Cell. Biol.*, 2007, **27**, 1007–16.
33 S. S. Myatt and E. W.-F. Lam, *Nat. Rev. Cancer*, 2007, **7**, 847–59.
34 S. S. Myatt, M. Kongsema, C. W.-Y. Man, D. J. Kelly, A. R. Gomes, P. Khongkow, U. Karunarathna, S. Zona, J. K. Langer, C. W. Dunsby, R. C. Coombes, P. M. French, J. J. Brosens and E. W.-F. Lam, *Oncogene*, 2013, 1–14.
35 D. J. Kelly, PhD Thesis, Imperial College London, 2014.
36 M. Deng, Master of Medical Science Thesis, The University of Hong Kong, 2006.
37 L. J. Monteiro, P. Khongkow, M. Kongsema, J. R. Morris, C. Man, D. Weekes, C.-Y. Koo, A. R. Gomes, P. H. Pinto, V. Varghese, L. M. Kenny, R. Charles Coombes, R. Freire, R. H. Medema and E. W.-F. Lam, *Oncogene*, 2012.
38 S. Padilla-Parra, N. Audugé, H. Lalucque, J.-C. Mevel, M. Coppey-Moisan and M. Tramier, *Biophys. J.*, 2009, **97**, 2368–76.
39 T. Nakamura, K. Aoki and M. Matsuda, *Methods*, 2005, **37**, 146–53.
40 V. Vasioukhin, in *Adherens Junctions: from Molecular Mechanisms to Tissue Development and Disease*, ed. T. Harris, Springer Netherlands, Dordrecht, 2012, vol. 60, pp. 379–414.
41 J. M. Brandner, M. Haftek and C. M. Niessen, *Open Dermatol. J.*, 2010, **4**, 14–20.
42 E. Sprecher, R. Bergman, G. Richard, R. Lurie, S. Shalev, D. Petronius, Shalata, Y. Anbinder, R. Leibu, I. Perlman, N. Cohen and R. Szargel, *Nat. Genet.*, 2001, **29**, 134–6.
43 J. E. Lai-Cheong, K. Arita and J. A. McGrath, *J. Invest. Dermatol.*, 2007, **127**, 2713–25.
44 E. Sahai and C. J. Marshall, *Nat. Rev. Cancer*, 2002, **2**, 133–42.
45 A. Hall, *Biochem. Soc. Trans.*, 2012, **40**, 1378–82.
46 D. R. Cook, K. L. Rossman and C. J. Der, *Oncogene*, 2013, 1–15.
47 J. McCormack, N. J. Welsh and V. M. M. Braga, *J. Cell Sci.*, 2013, **126**, 379–91.
48 N. J. Welsh, PhD Thesis, Imperial College London, 2013.
49 A. S. Yap and E. M. Kovacs, *J. Cell Biol.*, 2003, **160**, 11–6.
50 S. A. Kim, C.-Y. Tai, L.-P. Mok, E. A. Mosser and E. M. Schuman, *Proc. Natl. Acad. Sci. U. S. A.*, 2011, **108**, 9857–62.
51 R. Kalaji, A. P. Wheeler, J. C. Erasmus, S. Y. Lee, R. G. Endres, L. P. Cramer and V. M. M. Braga, *Biol. Cell*, 2012, **104**, 435–51.
52 R. E. Itoh, K. Kurokawa, Y. Ohba, H. Yoshizaki, N. Mochizuki and M. Matsuda, *Mol. Cell. Biol.*, 2002, **22**, 6582–6591.
53 H. Yoshizaki, Y. Ohba, K. Kurokawa, R. E. Itoh, T. Nakamura, N. Mochizuki, K. Nagashima and M. Matsuda, *J. Cell Biol.*, 2003, **162**, 223–32.
54 S. J. Heasman, L. M. Carlin, S. Cox, T. Ng and A. J. Ridley, *J. Cell Biol.*, 2010, **190**, 553–63.
55 H. Yoshizaki, Y. Ohba, K. Kurokawa, R. E. Itoh, T. Nakamura, N. Mochizuki, K. Nagashima and M. Matsuda, *J. Cell Biol.*, 2003, **162**, 223–32.
56 V. M. M. Braga and A. S. Yap, *Curr. Opin. Cell Biol.*, 2005, **17**, 466–74.
57 G. Izumi, T. Sakisaka, T. Baba, S. Tanaka, K. Morimoto and Y. Takai, *J. Cell Biol.*, 2004, **166**, 237–48.
58 B. Baum and M. Georgiou, *J. Cell Biol.*, 2011, **192**, 907–17.
59 A. Togawa, J. Sfakianos, S. Ishibe, S. Suzuki, Y. Fujigaki, M. Kitagawa, I. Mellman and L. G. Cantley, *Biochem. Biophys. Res. Commun.*, 2010, **400**, 271–7.
60 N. Lamarche-Vane and A. Hall, *J. Biol. Chem.*, 1998, **273**, 29172–7.
61 D. P. LaLonde, M. Grubinger, N. Lamarche-Vane and C. E. Turner, *Curr. Biol.*, 2006, **16**, 1375–85.
62 K. Makrogianneli, L. M. Carlin, M. D. Keppler, D. R. Matthews, E. Ofo, A. Coolen, S. M. Ameer-Beg, P. R. Barber, B. Vojnovic and T. Ng, *Mol. Cell. Biol.*, 2009, **29**, 2997–3006.
63 J. J. McCormack, PhD Thesis, Imperial College London, 2013.
64 A. Chatterjee, L. Wang, D. L. Armstrong and S. Rossie, *J. Biol. Chem.*, 2010, **285**, 3872–82.
65 M. Zuker, A. G. Szabo, L. Bramall, D. T. Krajcarski and B. Selinger, *Rev. Sci. Instrum.*, 1985, **56**, 14–22.
66 T. Nakabayashi, H.-P. Wang, M. Kinjo and N. Ohta, *Photochem. Photobiol. Sci.*, 2008, **7**, 668–70.
67 K. J. Hodivala and F. M. Watt, *J. Cell Biol.*, 1994, **124**, 589–600.
68 S. S. Vogel, T. A. Nguyen, B. W. van der Meer and P. S. Blank, *PLoS One*, 2012, **7**, e49593.
69 Micro-Manager Open Source Microscopy Software, *https://www.micro-manager.org/, (accessed January 2015)*.

